

AN ABSTRACT OF THE THESIS OF

Alexander Muschler for the degree of Master of Science in Mechanical Engineering presented on December 5, 2018.

Title: Ground Gen Airborne Wind Energy Conversion Systems: Tools for Conceptual Design and Rapid Prototyping

Abstract approved: _____

Roberto Albertani

Airborne Wind Energy System (AWES) are quickly coming to fruition, with increased energy production while reducing the cost of implementation and materials. This thesis develops a new computational model for a tethered AWES and characterizes a new rapid prototyping method with the objective of supporting the design and rapid prototyping complex geometries to increase stiffness and strength. Vortex lattice method (VLM) code efficiently estimated the aerodynamic coefficients and wind tunnel tests showing little discrepancy from the VLM model. The power model showed similar results to other researched models from Myles Loyd, and Fchener. Furthermore, the model showed that a bridle can add a significant increase in pitch stability and the ability to increase pitch authority without a horizontal stabilizer. Wind tunnel results confirm high lift capabilities of the delta wing geometry with angle of attack up to 90° , although the power generation is not optimal due to the small aspect ratio of the main element. Using 3D printed nylon (PA12) and carbon fiber reinforced polymer (CFRP), thermal and mechanical properties were characterized to determine the feasibility of using the 3D printed structure as a core and a mold. It was determined that the weight percent composition of the PA12 had about 1.5% water and 14% carbon platelet, which the water can adversely affect chemical adhesion and the carbon improves mechanical properties. Additionally, the PA12 also had the thermal stability

to withstand the cure temperatures of the CFRP. Through tensile tests, it was determined that within the linear region the PA12 exhibited isotropic behavior. However, for ultimate failures, the PA12 exhibited anisotropic behavior, using the coordinate system of the 3D printer, with the X direction absorbing 2.4 times more energy with a higher strain and ultimate failure. It was shown that stronger adhesion occurred between the PA12 and the CFRP using a lower cure temperature and vacuum. The lower temperature avoids residual stresses caused by the difference in coefficient of thermal expansion. The adhesion strength verified that the 3D printed PA12 structure can be used as a core and mold for rapid prototyping applications. Further development of AWES are then discussed.

©Copyright by Alexander Muschler
December 5th, 2018
All Rights Reserved

Ground Gen Airborne Wind Energy Conversion Systems: Tools for Conceptual Design
and Rapid Prototyping

by
Alexander Muschler

A THESIS

submitted to

Oregon State University

in partial fulfillment of
the requirements for the
degree of

Master of Science

Presented December 5, 2018
Commencement June 2019

Master of Science thesis of Alexander Muschler presented on December 5, 2018

APPROVED:

Major Professor, representing Mechanical Engineering

Head of the School of Mechanical, Industrial and Manufacturing Engineering

Dean of the Graduate School

I understand that my thesis will become part of the permanent collection of Oregon State University libraries. My signature below authorizes release of my thesis to any reader upon request.

Alexander Muschler, Author

ACKNOWLEDGEMENTS

Academic:

I'm indebted to:

- eWind Solution
- Oregon Best
- US Department of Agriculture
- Rapid Made

As these organizations have provided funding and support that made this research possible.

Personal:

I would like to thank my advisor Dr. Roberto Albertani for his un-wavering support and willingness to answer questions throughout my time at Oregon State University. Additionally, I express my gratitude to my committee members Dr. John Parmigani and Dr. Brian Bay who, through course work, have provided me the foundation required to make this research possible. I would also like to acknowledge the experience provided to me through Global Formula Racing Team and the Society of Automotive Engineers (SAE), which has proven invaluable by providing a fast-past learning environment and hands on learning experience. My lab mates and team members also have my gratitude, as they have motivated me and provided a strong support network throughout my master's program. Finally, I would like to thank my family and friends for the support throughout this process, especially; John Muschler, Heidi Feiler, Evan Muschler, Michael Feiler, Audrey Muschler, Heidi Owens and Abby Schamp. As they provided me with their guidance, wisdom and support.

CONTRIBUTION OF AUTHORS

Contributions in Chapter 2

Acknowledge: Dr. Albertani for his counsel throughout the project. Nathaniel Brent Osterberg for his instruction on the wind tunnel testing and collaboration on the power generation model.

Contributions in Chapter 3

Acknowledge: Dr. Albertani for his counsel throughout the project.

TABLE OF CONTENTS

	<u>Page</u>
1. MOTIVATIONS OF RESEARCH	1
2. INTRODUCTION.....	2
2.1 BACKGROUND INFORMATION.....	3
2.1.1 THE PROBLEM.....	3
2.1.2 CROSSWIND ENERGY GENERATION.....	4
2.1.3 CLASSIFICATION OF AWES	6
2.1.4 CURRENT AWES	9
2.1.5 RIGID WING PUMPING CYCLE AWES	11
2.2 LITERATURE REVIEW.....	13
2.2.1 Airborne Wind Energy Systems.....	13
2.2.2 Composite Structures and Design	20
2.2.3 Additive Manufacturing	23
2.2.4 Hybrid Manufacturing.....	27
3. PERFORMANCE OF A TETHERED AIRBORNE WIND ENERGY SYSTEM	31
3.1 NUMERICAL MODEL.....	31
3.1.1 Tornado (Vortex Lattice Method).....	32
3.1.2 Power Generation Model.....	42
3.1.3 Performance Characteristics.....	49
3.2 WIND TUNNEL STUDY	57
3.2.1 Experimental Setup	57
3.2.2 Results	59
4. THERMAL AND MECHANICAL TESTING OF CARBON FIBER REINFORCEMENT	60
4.1 THERMAL CHARACTERIZATION OF PA12.....	64
4.1.1 Thermogravimetric Analysis (TGA).....	64
4.1.2 Digital Scanning Calorimetry (DSC).....	68

TABLE OF CONTENTS (CONTINUED)

	<u>Page</u>
4.2 TENSILE TESTS.....	73
4.2.1 Experimental Setup	75
4.2.2 Results	77
4.3 DOUBLE LAP JOINT TESTS	79
4.3.1 Experimental Setup	80
4.3.2 Results	83
5. SUMMARY AND CONCLUSION	85
5.1 FUTURE WORK.....	88
REFERENCES.....	90
APPENDIX	96
APPENDIX A: DERIVATION OF PITCH STABILITY EQUATION.	96

LIST OF FIGURES

<u>Figure</u>	<u>Page</u>
Figure 2.1: Image comparing conventional wind turbines to the increased efficiency of an AWES.	5
Figure 2.2: Three primary configurations of AWES configurations a) On board Power Generation using Makani's initial prototype b) traction power using Ampyx geometry c) Lighter than air configuration by Altaeros Air ^{11 12 13}	6
Figure 2.3: Crosswind flight generation system using the figure eight flight pattern.	11
Figure 2.4: The energy generation per unit area based on wind speed, the ratio of coefficient of lift and coefficient of drag.	12
Figure 3.1: Delta wing configuration and geometric variables.....	37
Figure 3.2: ASK 21 glider geometry.....	39
Figure 3.3: Delta wing geometry.	40
Figure 3.4: Convergence study of the coefficient of lift and drag for the increased mesh density.	41
Figure 3.5: Loading conditions due to aerodynamic	53
Figure 3.6: Stability of the Delta wing geometry A) pitch stability with bridal, tail length and area ratio. B) without the effects of the bridal.....	55
Figure 3.7: Stability of an aircraft based on bridal geometry dependent on the bridal angle using a CG offset of 0.01 meter.	56
Figure 3.8: The Oregon State University closed loop wind tunnel with stunt kite test geometry. 58	
Figure 3.9: Angle of attack sweep vs coefficient lift.	59
Figure 3.10: Drag polar of delta wing configuration.	60
Figure 4.1: Toray 2510 semi toughened out of autoclave (OOA) epoxy cure cycle which offers a curing rage from 250 to 270 degrees F or 121 to 132 degrees Celsius ⁸⁸	62
Figure 4.2: plot of thermogravimetry to determine the weight percent composition of PA12, carbon black, and other	68
Figure 4.3: Differential Scanning Calorimetry Q 2000 series used to measure the exothermic and endothermic response of the polymer.	71
Figure 4.4: Differential scanning calorimetry slow cooled plot showing the glass transition temperature, the melting temperature and the crystallization temperature.	72

LIST OF FIGURES (Continued)

<u>Figure</u>	<u>Page</u>
Figure 4.5: RapidMade's 4200 series processing station for HP's PA12 parts which recycles un used PA12 and results in high tolerance parts.....	75
Figure 4.6: Experimental setup for tensile tests of PA12 samples in the Instron	76
Figure 4.7: Graph of both the X and Y direction comparing the stress and strain. As shown, the X direction and Y direction have similar mechanical properties in the linear region and the ultimate tensile strengths.....	77
Figure 4.8: An example of how the PA12 samples fractured during testing. The fractures were very brittle and resulted in material breaking off the sample.....	79
Figure 4.9: Experimental dimensions for double lap joint test (ASTM D 3528)	81
Figure 4.10: Manufacturing process using a Renshape mold to layup on and vacuum.....	82
Figure 4.11: Double lap joint sample mounted in the Instron	82
Figure 4.12: Average axial stress within the PA12 A) bonded at a 121°C cure with vacuum B) bonded at a 130°C cure with vacuum C) bonded at a 130°C cure with no vacuum	83
Figure 4.13: Fractured double lap joint specimen with a 250 cure and 1 atmosphere of vacuum pressure.....	84
Figure 4.14: A) The porous surface finish of the PA12 using 10X objective lens. B) The bond interface between the epoxy resin system and the PAS12 showing diffusion at the surface using a 10X objective lens.	85

LIST OF TABLES

<u>Table</u>	<u>Page</u>
Table 2.1: Current commercial AWES and the status in which they have their system.	10
Table 3.1: The power generation of the Delta Wing and ASK21 Glider with 5, 10, 15, and 20 m/s winds. The results are compared to Loyd's lift model.	48
Table 4.1: The composition of the PA12 3D printed parts determined using the TGA.	68
Table 4.2: Thermal characterization of the PA12 using the DSC.	72
Table 4.3: Shows the mechanical properties of the 3D printed specimens based on the direction they were printed and the statistical evaluation of the results.	78
Table 4.4: Mechanical properties of the double lap joint specimens using the three different cure process.	84

NOMENCLATURE

<i>Symbol</i>	<i>Units</i>	<i>Description</i>
<i>Aerodynamic Coefficients</i>		
A	m^2	Wing area
AR	Unitless	Aspect ratio- the
C	N	Drag Reference Frame of the Aircraft
C_D	Unitless	Coefficient of Drag
C_{D_i}	N	Induced Drag
$C_{D,eff}^t$	N	Effective Tether Drag
C_L	Unitless	Coefficient of Lift
d	m	Length of Tether
dC_m/dC_L	Unitless	Slope of the Pitching Moment
F_{\perp}	N	Forces Perpendicular to Free Stream
F_{\parallel}	N	Forces Parallel to Free Stream
F_L	N	Aerodynamic Lift
l	m	Length of the Cross-span Vortex
L	N	Local Lift
N	N	Lift Reference Frame of the Aircraft
q	Pa	Dynamic Pressure
S	m^2	Wing Surface Area
V	m/s	Free Stream Velocity
v_a	m/s	Apparent Aircraft Velocity
V_w	m/s	Wind Velocity
x	m	Distance from Center of Gravity (CG)
ρ	Kg/m^3	Density of the Air
Γ	m/s	Vortex Strength
<i>Mechanical and Thermal Coefficients</i>		
f	<i>Unitless</i>	Filler Fraction
ΔH	J/g	Enthalpy
T_g	$^{\circ}C$	Glass Transition Temperature
T_m	$^{\circ}C$	Glass Transition Temperature
O	mg	Medium Volatile Mass at Specific temperature Range
V	mg	Highly Volatile Mass at specific Temperature

1. Motivations of Research

The motivations of this research are to develop new numerical methods that accurately model Airborne Wind Energy System (AWES) and rapidly prototype different geometries to validate the models. Main design features when developing AWES are the geometry of the aircraft and their effects on the energy generation and the flight characteristics. These difficulties include the launching and landing of the air vehicle, keeping the system under control through a wide variety of environmental situations, and maintaining high strength to weight ratios. Additionally, to achieve a successful system, extensive prototyping needs to be conducted with many of the most promising systems already at their 4 or 5 full system prototypes.

For AWES to be a reality, different aircraft geometries need to be defined, simulated, prototyped, and tested. The research that follows is integral to the concept design and prototyping of an AWES as it contributes a numerical model with high degree of geometric flexibility, provides a new pitch stability model, and conducts a wind tunnel study on an aircraft with near vertical takeoff capabilities. The numerical model uses a time efficient MATLAB simulation, allowing initial concepts to be iterated through rapidly by using the vortex lattice method (VLM). VLM then determines the basic aerodynamic coefficients, which can be used in the fixed stick pitch stability model. A new numerical model is derived for the pitch stability with a bridled system. In parallel, a unique delta wing geometry is tested in the wind tunnel, exploring the effects of high angle of attack lift for applications during takeoff and landing. The Delta wing geometry allows the aircraft to takeoff without relying on a launch system, increasing the reliability and reducing the cost of the system.

Prototyping has quickly proven to be the most critical step for the development of AWES, an area where many startups fail. Fixed wing prototypes are difficult to manufacture and iterate in a rapid and cost-effective manner, especially when the primary material used for fixed wing prototypes is fiber reinforced polymers (FRP). A considerable amount of the time and cost associated with composite manufacturing is tooling. This is especially difficult when implanting composites as you will most likely need a new mold for slight geometry adjustment. The research that follows has developed a new manufacturing technique that allows the 3D printed structure to serve a dual purpose as a core and as a mold surface for composite sandwich panel. By combining 3D printing and composites this manufacturing technique allows complex geometries such as airfoils to be generated rapidly with high specific strength and stiffness. This research shows that PA12 and composite laminate's thermomechanical properties allow the 3D printed core structure to be bonded well to the face sheets of the composite structure using epoxy film adhesive. This approach negates costly mold manufacturing procedures and allows composites to be rapidly prototyped, creating one off design that weren't previously achievable.

2. Introduction

AWES are an airborne system which generates energy from the wind. A form of renewable energy, AWES are trying to lower our populations reliance on fossil fuels. These systems have the potential of being more efficient than conventional wind turbines by accessing higher energy dense winds and reducing cost of implantation. Through a diversity of proposed systems there have two companies which have succeeded in developing autonomous prototypes however with prototyping proving critical they are still in the development phase. Only one of the companies have succeeded in generating energy with a full-scale prototype.

2.1 Background information

The background focuses on defining the problem and how an AWES solves it. A discussion on how the system generates energy, comparing the theoretical energy output to current conventional green energy systems. Different configurations of AWES systems are evaluated along with the status of current startups exploring this technology. Then AWES configuration that this research focuses on is then defined.

2.1.1 The Problem

Societies ability to progress while sustaining large populations, depends on the amount and type of energy available .¹ Because a majority of our energy is derived from fossil fuels, there exists severe issues regarding the extraction, transportation, by-products, and sustainability that negatively affect our environment. This has resulted in major countries investing in renewable energy and enacting green energy polices. For example, in September 2009, both the European Union and the G8 leaders agreed to reduce carbon dioxide emissions by 80% before 2050 .² The need for electrical energy which can be generated without affecting our current environment proves to be critical to accomplish the emission reduction goals and in last decade, a large increase in renewable energy projects came online, with wind turbines and solar panels showing the largest growth. As investment continues, focus shifted toward increasing the unit power per unit land area, through increased efficiency. This focus leads to larger turbine blades and towers, increasing the overall efficiency, but significantly increases the cost of materials. ^{3,4}

AWES are quickly coming to fruition within the modern world, increasing energy compared to cost of implantation. AWES are defined as a new renewable energy sector, aiming to collect wind energy within the ranges of 200 m to 10 km from the earth's surface. ⁵ Consisting of a

variety of configurations, AWES are mechanically attached to the ground. Energy is generated through traction forces caused by aerodynamic loads, which are then turned into electrical power. The three major reasons AWES are being researched are: ⁶

1. Similar to solar, wind power is potentially capable of generating enough energy to satisfy all of humanity's energy needs.
2. When compared to ground-based wind turbines, AWES can achieve higher altitudes, thereby reaching more energy dense wind currents such as jet streams, which have been untouched. These winds are more consistent and stronger than what is typically seen on and off shore.
3. AWES require significantly less material investment per unit of usable energy, and therefore generating a large power to mass ratio. The large power to mass ratio allows the potential of large-scale development at comparably low cost compared to other renewable energies.

2.1.2 Crosswind Energy Generation

AWES use crosswind kite power to drive electrical generators. This power is easily exhibited by the high speed and aerial maneuvers that recreational kite surfers perform on the water.

Crosswind kite power was coined by Miles Loyd in 1980. When Miles Loyd modeled the maximum energy that could be generated through a cross flight AWES, he provided the basic foundation for two different power generation systems, lift mode and drag mode. Lift mode uses tether tension to drive a ground-based turbine, while drag mode uses the high apparent airspeed of the aircraft to drive turbines mounted to the aircraft. ⁷

Developers often directly compare crosswind kite power energy systems and ground-based wind turbines, as shown in Figure 2.1. From this perspective, the AWES represent the most external part of the wind turbine blade, or the fastest moving part. The outer 30% of the blade generates more than half of the total power from a wind turbine. An AWES replaces an entire turbine tower with a tether and a blade that has an automated flying wing, which can be much lighter and thinner than the required construction of a turbine blade.^{8,6,5}

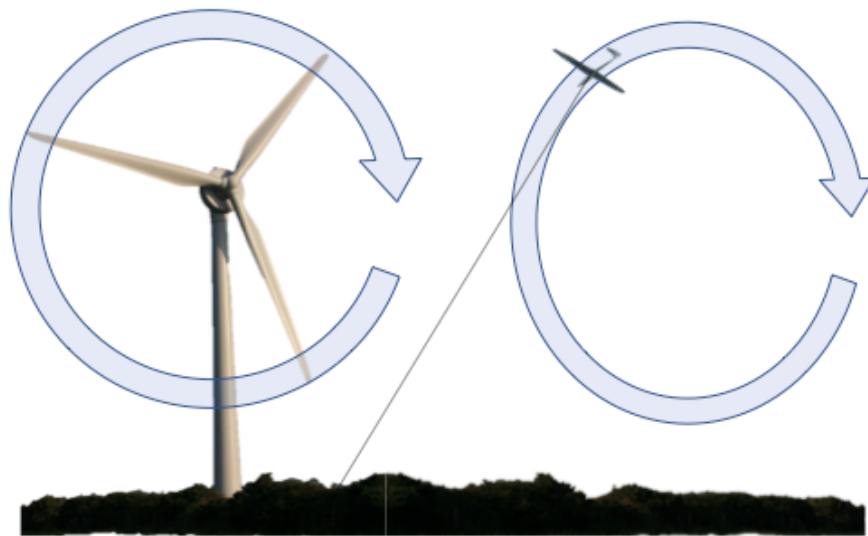


Figure 2.1: Image comparing conventional wind turbines to the increased efficiency of an AWES.

Using Myles Loyd's initial power generation function, discussed further in the literature review, with an aircraft with a coefficient of lift (CL) of 1, coefficient of drag C_D of .07, and wind velocity of 13 m/s can theoretical output of 40 kW per m^2 . When comparing this power density to that of photovoltaic cells, the density of solar irradiation is 1.3 kW per m^2 at 20% efficiency. Showing the power density per meter squared of wing area is more than 154 times than that of commercial photovoltaic cell. Through these basic models, the benefits of large power generation with a significant reduction in infrastructure become evident.⁶

2.1.3 Classification of AWES

From Myles Loyd's initial lift and drag models, different classifications of AWES have been defined. These classifications depend on how power is generated and the physical characteristics of the aircraft, defined by: On-board Power Generation, Ground Based Power Generation, Vehicle Propulsion, Flexible vs Rigid Wings, Multi Wing Systems, and Lighter than Air, as shown in Figure 2.2. ^{5,8,9,10}

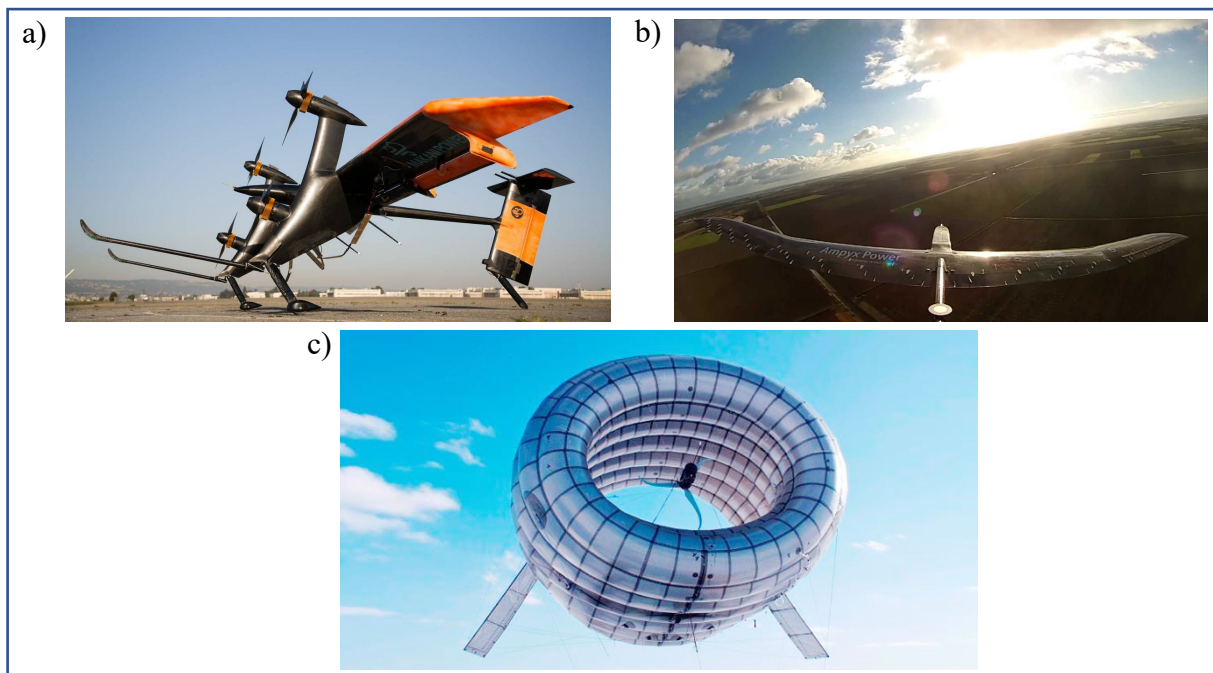


Figure 2.2: Three primary configurations of AWES configurations a) On board Power Generation using Makani's initial prototype b) traction power using Ampyx geometry c) Lighter than air configuration by Altaeros Air ^{11 12 13} .

On-board Power Generation correspond to Loyd's drag model, that fast flying tethered aircrafts use fixed turbines on the aircraft to generate the power. The advantages of such a system include the turbines reaching high rotational speeds, allowing them to generate electricity without a gearbox. This method, used by Makani a Californian startup, also uses the on-board rotors as a launching mechanism. Disadvantages of such a system include increased drag caused by the turbines, and the additional weight of the tether and turbines. The tether also needs to perform the dual function of conducting electricity to the ground while withstanding strong tensile loads of the aircraft. ¹⁴

Ground Based Power Generation, or traction power generation, uses the strong lift forces from the aircraft to unroll a ground-based drum. The action of unrolling the drum drives an electrical generator mounted to the ground. By Combining crosswind motion and ground-based energy generation, this classification corresponds the best with Loyd's lift mode. The process consists of two different phases, a power production phase, known as the reel out phase, and the reel in phase. In the reel out phase, the aircraft flies a specified flight path, increasing aerodynamic loads, and pulls the tether out, in turn rotating the drum and driving the generator. The aircraft stalls in the reel in phase and adjusts so that the minimal amount of energy is required to draw the aircraft to its initial starting position of the reel out phase. This process of power generation is often defined as the pumping cycle. The advantages to such a system include an extremely low weight per square meter of the airborne system. Two common aerodynamic wings that are used for such a system are: lightweight flexible wings and rigid wings similar to high performance sail planes. The main difficulty of such systems is the automated control, as they require more control lines and a more complex flight path compared to other systems. Loyd's lift model shows the most promise because an aircraft using a rigid wing with high lift and low drag can minimize energy loss through the system.

Instead of converting the energy of AWES to electrical, some studies have been devoted to using them for the propulsion of a vehicle. The first patented AWES was a kite drawn buggy that was patented by George Pocock in 1827.¹⁵ Although AWES are primarily concerned with the development of electrical generation, the naval vehicle propulsion market can also benefit from airborne propulsion systems. Very similar to traction-based energy generation, this configuration can play a critical part in the development of AWES.

A large division within AWES literature is whether to use flexible wings, similar to that of kite surfers, or rigid wings, like that of a high-performance glider. Flexible wings can be extremely light and hold their aerodynamic shape from the air pressure, allowing them to fly at moderate speeds and be easily controlled by a humane pilot. Rigid wings keep their shape and have a higher coefficient of lift to drag ratio but are heavier per square meter. As a result of the higher coefficient of lift to drag ratio, rigid wings can reach higher speeds but are more difficult to control. Due to the higher speeds reached by the rigid wing, the loads are much larger, giving a significantly higher power output per wing area, increasing the efficiency. The higher speeds create higher apparent wind velocity, which increases the aerodynamic forces. As shown below, using the equation for aerodynamic lift.

$$F_L = \frac{1}{2} \rho v_a^2 A C_L$$

The ρ is the density of the air, A is the area of the airfoil, C_L is the coefficient of lift of the aircraft, and v_a is the apparent wind speed. If an aircraft is flying at 10 times the speed of the wind, the tensile strength on the tether would be 100 times stronger. When compared to static systems, the energy potential is much higher using the kinetic energy of a kite.

Another configuration includes using multiple wings to combat tether drag. To reach high altitudes, a long tether is required; however, with such a long tether, the drag produced becomes a significant factor that reduces the efficiency of the system. When using a multiple kite system, the tether can be broken up into two partitions: a primary tether fixed to the ground and a secondary tether that connects the aircraft to the primary tether. Such a system does significantly reduce tether drag; however, power does not increase linearly with the addition of wing elements. With the addition of wing elements, they can begin to affect the airflow around each

other. The affected flow is similar to wing wash, occurring when by trailing elements have reduced stability from the turbulent flow of the main element. The main difficulties of such a system are the startup and low reliability of the system, resulting in no current large-scale multiple wing AWES prototype. ^{5,8,16}

The last classification of AWES are lighter than air systems. Rather than using aerodynamic lift to keep the aircraft aloft, the system relies on its buoyancy force. Such systems are similar to Loyd's drag model but are stationary, like current ground-based turbines. These systems rely on keeping a generator airborne along with the turbine while also using the tether to transmit the energy to ground, keeping it fixed. By not relying on the wind to stay aloft they can stay airborne indefinitely without using energy; however, this comes at a significant cost. Such systems require large volume and helium to generate enough buoyancy to offset their weight. The large volume required acts as a fundamental design limitation and has resulted in them not coming to fruition. ¹⁷

2.1.4 Current AWES

With the energy potential of AWES, a large variety of startup companies have attempted to bring them to market in the last decade. Twelve startups have been able to generate an initial controllable prototype, but few have had success in creating autonomous energy generating systems as shown in the Table 2.1. The most successful startups have been Makani and Ampyx wind. Both created fully automated systems capable of generating energy. Makani's M600 is the fourth complete prototype and first large-scale energy generation system made by them. In December of 2016, the system was able to generate autonomous energy, making it one of the first large energy output systems to be produced. The M600 uses Loyd's drag system and has 8

turbines. Another startup, Ampyx, developed 8 prototype wings with the different prototype systems named AP0, AP1, and AP2 types. Ampyx’s prototypes use Loyd’s lift mode to generate energy. In 2012, with their AP1 system, they were able to have the first automated energy generation. Beginning in 2017, they began developing AP3 and AP4. AP3 is being used to develop safe automated launching and landing capabilities, to be completed in 2022, while the AP4 will be a 2 MW on-shore system. The AP4 will be the basis for the commercial off shore system and is predicted to be complete in 2024.

Table 2.1: Current commercial AWES and the status in which they have their system.

Company	System	Status	Country
<i>Altaeros</i>	Lighter than air system	Prototyping have an initial prototype	United States
<i>Ampyx Power</i>	Ground Based rigid wing using a pumping cycle	Autonomous power generating prototype. Increasing scale and safety working on 3 and 4 prototypes	Netherlands
<i>EnerKite</i>	Ground Based rigid wing using a pumping cycle	Basic autonomous prototype, designing 200kw prototype	Germany
<i>eWind</i>	Ground Based rigid wing using a pumping cycle	Prototyping and developing fully autonomous system	United States
<i>KiteGen</i>	Ground Based Flexible wing using a pumping cycle	Prototyping system	Italy
<i>Kitemill</i>	Ground Based rigid wing using a pumping cycle	Generating larger scale porotype has smaller scale prototype with autonomous system	Norway
<i>Kite Power BV</i>	Ground Based Flexible wing using a pumping cycle and Drag model	Prototyping 100 kW nominal system	Netherlands
<i>Kite Power Systems (KPS)</i>	Ground Based Dual Flexible wing system using a pumping cycle	Prototyping system predicted to have full scale system by 2023	United Kingdom
<i>Makani</i>	On-board power generation using fixed wing	Successful 600 kW prototype developing larger scale prototype	United States
<i>SkySails</i>	Vehicle propulsion system and ground based flexible wing system	400 m ² kite prototype used to propel ships and tested power system.	Germany
<i>TwingTec</i>	Ground Based Flexible wing using a pumping cycle and Drag model	Flying prototype, still in the prototyping phase	Switzerland

With a large diversity of global startups, many different systems are being generated. The prototype phase is proving to be the most critical stems for these systems. Successful companies have been able to test a variety of geometries, allowing them to have a successful system.

2.1.5 Rigid Wing Pumping Cycle AWES

With configuration defined, and the current AWES market described this research focuses the development of the most promising energy system which uses a rigid wing pumping cycle AWES. This configuration shows the most promise in efficiency and generating large amounts of energy, discussed further in the motivations section. Depicted below, the system uses cross wind flight in a figure eight pattern, as seen in Figure 2.3. The figure eight pattern generates high traction forces due to the increased the velocity of the aircraft, creating more energy while preventing control lines from becoming twisted.

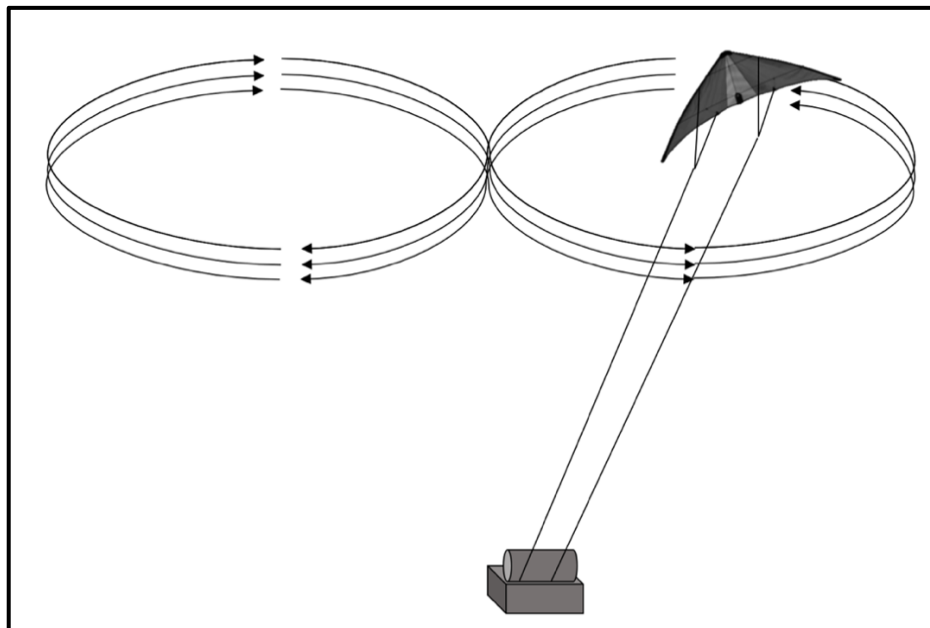


Figure 2.3: Crosswind flight generation system using the figure eight flight pattern.

The system's energy generation is best described by Loyd's initial lift model. Using Loyd's simplified model the power density per meter squared of wing area can be calculated using equation.

$$\frac{\text{Power}}{\text{wing area}} = 0.5 \rho V_w^3 C_L \frac{4}{27} \left(\frac{L}{D}\right)^2$$

This equation relies on the air density (ρ), wind velocity (V_w), coefficient of lift (C_L), and the lift to drag ratio ($\frac{L}{D}$). This simplified model is often referred as the maximum energy that can be generated by an AWES. When plotted, as in Figure 2.4, it shows the importance of the lift to drag ratio, coefficient of lift, and the wind velocity impact on the energy generation of the Airborne wind energy system.

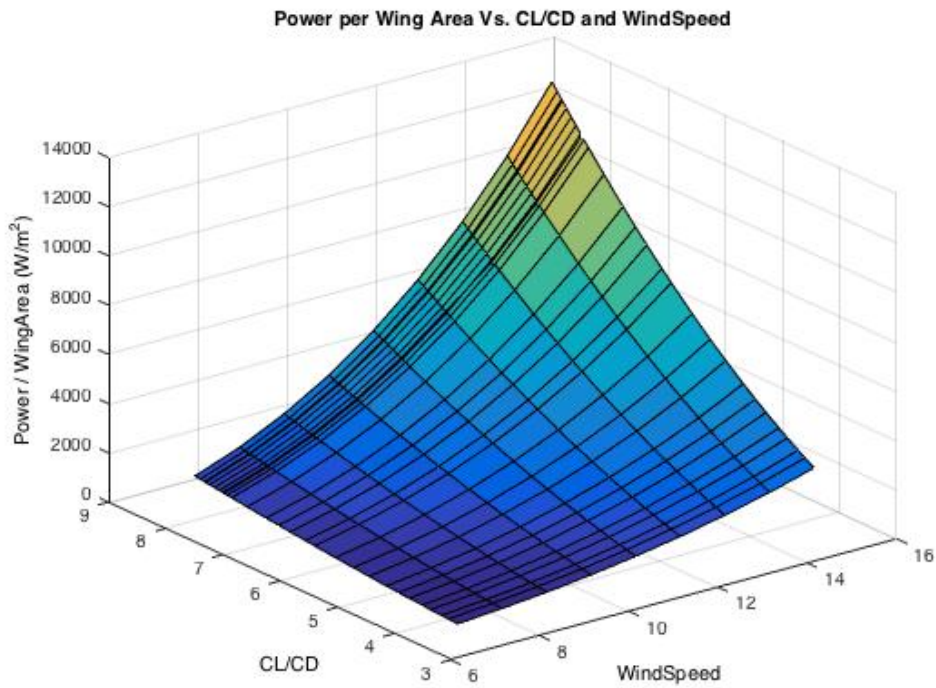


Figure 2.4: The energy generation per unit area based on wind speed, the ratio of coefficient of lift and coefficient of drag.

2.2 Literature Review

The literature is broken up into four different sections: 1) AWES 2) composite structures, 3) additive manufacturing 4) hybrid manufacturing.

2.2.1 Airborne Wind Energy Systems

Before 1970

1827 George Pocock invented and patented the Charvolant, a horseless drawn buggy that was propelled using a kite and proposed the use of kites for propelling ships. Although the Charvolant was proven to be difficult to control, it was the first proposed application of controlling and harvesting kite energy. His work with kites were also published in his book “The Aeropleustic Art or Navigation in the Air by the use of Kites, or Buoyant Sails”.¹⁵ Considered eccentric, the idea of using a kite to extract energy didn’t resurface again until the 1970’s.

1970-2000

In 1970, Myles Loyd, of the Lawrence Livermore National Laboratory, developed the first concept of modern Airborne Wind Energy Systems (AWES). In 1980, he published his seminal work providing the foundation for modern crosswind AWES, a term coined by Loyd. The paper analyzed the theoretical maximum energy of a tethered kite using three different flight systems: 1) static release of the kite, which simply pulls the tether; 2) crosswind flight and; 3) drag induced power using turbines. His more complex model took into consideration the tether’s drag, kite motion projected on a sphere and the weight of the tether, and with an efficiency of 33%, the model identified tether drag as a limiting factor for AWES. Using a coefficient of lift of $C_L=1$ and a coefficient of drag $C_D=0.07$, he found a theoretical power output of $P = 40 \text{ kW per m}^2$. Though this power density has yet to be experimentally proven, it has been confirmed through more advanced computer simulations.^{6,7,18} Loyd’s work was followed by Wellicome et al. who

studied the prospects of using wind assisted devices on merchant ships to reduce fuel consumption in the 1980. The study focused on relative size of the specified aircraft to increase efficiency by using aerodynamic loads as a driving force. Vital parameter for a transportation system were relationship between vehicle speed and wind speed, and maximum lift. After Loyd's and Wellicome's seminal projects, AWES research was abandoned in then nineties.¹⁹

2001-2005

The early 2000's more energy generation simulations were derived, many using Loyd's work as a basis. Moritz Diehl et al. developed the next kite model in 2005. The model starts from an arbitrary initial state and then steers the kite into periodic orbit of a figure eight pattern. This model is the first model that took into account the flight path and used a figure eight while also considering the mass of the aircraft and tether length.²⁰

2006-2010

In 2006, Canale et al. developed the first study researching the control of an AWES using a two-line system. Using predeveloped power generation simulation, they computed the mean time required for computation of control, which is about 0.01s, largely lower than the required sampling rate of .1s. This simulation didn't accurately factor dynamic effects of the aircraft.¹⁴ In 2007 Paul Williams et al. developed a power model which the kite system is applied to a large lever arm creating torque on the generator. Though the generator system explored wasn't conventional, they discovered the optimal kite trajectory follows a cross-wind pattern. For low wind speed and kite areas, the flight path is an elongated ellipse in the normal plane. Also, this research demonstrated that the power generation is proportional to the kite area and the cube of the wind speed.²¹ In 2009, Argatove et al. developed a numerical model for a pumping kite. Similar to Loyd's crosswind flight generator, which flies at high cross wind speeds. Once max length is reached the kite is stalled and is retracted completing the pumping cycle. The Argatove model utilized a dual control line kite and took into consideration the period of the periodic

motion, the resulting lift-drag of the tether, strain of the tether and the static line profile of the tether. The results show a mean power of 5.7 MW given the same constraints as Diehl's which was 4.9 MW. The development of these model continued well into the next decade.^{20,22}

2010-2015

In 2010 J. Kim and C. Park proposed idea of using a parawing to draw a large ship. Using similar methods to Diehl M and Argatov et al. the power density of the kite is estimated for a moving vessel.^{20,22,23} Using multi body dynamics, Jeroen Breukels in 2010, generated a model which considers rotational inertia as well as multi body dynamics. He concluded that coupling a structural finite element analysis to a computational fluid dynamics analysis to fully simulate a complete kite is not feasible for a kite simulation tool. The model showed a strong correlation to experimental results done with a kite surfer wing. The inaccuracies between the experimental and the model was believed to have been due to the difference in airfoil thickness of 5%. The tether drag was more accurate due to it being segmented rather than perfectly stiff.²⁴ In 2011, Miller L. M. analyzed the wind energy density of high-altitude jet streams with velocities greater than 25 m/s. The research predicts a conservative estimate of 7.5 TW of energy being able to be drawn from the atmosphere.²⁵ George M. Dadd also published a 2011 document on predicting the time average aerodynamic forces and pragmatizing the figure eight kite trajectories while also comparing loads and the time scale to experimental validation. The results did show that the theoretical time for the kite to progress around the maneuver closely matches that of the experimental kite trajectory with largest errors being due to differences in wind speed across the flight envelope. The simulation uses the equations previously derived from George M. Dadd kite models in 2010. The results also show, similar to aircrafts, a large increase in loading with an increase in aspect ratio and that figure eight shape kite trajectories centered on an elevation around 15 degrees is preferred to maximize the tether loading.²⁶ In 2011, Argatov made further

improvements to the model showing that drag had more significant effect by including the tether sag. The largest conclusions that can be drawn from this paper is that 1) influence of the kite's lateral control angle on the tangential kite dynamic is negligible 2) the combined effect of kite's control and gravity is relatively small compared to the kite's inertia 3) the tether's drag from the previous model had an error of a few percent which were a cause of the tether's system parameters.²⁷ In 2012, the first autonomous flight of a rigid wing system was flown by Ampyx Power using their AP1 prototype.¹¹ In 2012, Stefan Haug was first to analyze a launch and retrieval system for an AWES specified for TU Delfts systems. His results showed a reduction in stability of the aircraft due to a short tether.²⁸ In 2012, the first wind tunnel study was done based on a tethered rigid wing. Conducted by Rogelio Jr. et al. the tethered wing used control surfaces called spoilers to stabilize and adjust the angle of flight. The aircraft used a bridle system to transfer energy, control the angle of attack, and transfer aerodynamic loads. The system used Loyd's static release system, which does not use cross wind energy. The control model and ability to measure position and generated energy using a dynamometer was successful. With the introduction of spoilers, severe oscillations within the system were minimized, as long as higher air speeds were not met, and minimum angle of attack of 5 degrees was required to generate energy. These tests represent the first-time a scaled model produced energy during a controlled flight.²⁹ Leo Goldstein used a modified version of Loyd's power model. The flight system uses general control tethers and then a tether which is directly attached to a generator, directly below the aircraft. This system showed the ability to harvest crosswind energy with two different basic theoretical calculations and more importantly a basic cost analysis was done. The AWES is around 10 times less expensive than a conventional wind turbine in terms of cost per kWh.³⁰ Costello et al., in 2013, used the zero-mass model from Dadd et al. 2010 for trajectory optimization of an AWES. The goal was to develop a real time optimization which can provided

the optimal operation despite uncertainty in flight conditions. Through this system the flight pattern was optimized and shown to be an oval like shape due to the force vectors. This is the first step to an iterative process of optimizing the flight, and correcting for perturbations.³¹ In 2013, Francesco Castellani and Alberto Garinei analyzed the possibilities of harnessing high wind potential through the use of an innovative airship. They took in consideration the topography of the terrain and optimal height for energy generation. The results show that optimal height can be affected by strong wind variations in wind direction in complex terrain sites, making height control of the aircraft important. While in flat terrain, the operating level only needs to be adjusted when thermals effect wind shear. According to meteorological models the recommend operating level seem to be 1 km above ground.³²

In 2014, J. Coleman et al. provided a full system break down to have a fully operational off shore AWES farm. Breaking it down into multiple components: 1) power take off 2) recovery system 3) direct interconnection 4) full scale power converter 5) synchronization of the routine. This system analyzed the first multiple AWES, or farm, in parallel connection showing that it can provide continuous power with an additional analysis provided of certain fault conditions.³³

Cristina L. Archer et al. provided a full climate analysis for airborne wind energy farms where consistent high wind speeds are found at lower altitudes, minimizing the drag induced by the tether. The criterion used was winds greater than $10 \frac{m}{s}$, occurring at least 15% of the time each month, and heights 3000 meters above ground level. Locations identified with the highest wind power densities consist of U.S. Great Plains, oceanic regions near the Hadley cells, and the Somali jet. The research showed that there are more wind speed maxima than previously thought.³⁴

Mario Zanon et al. further refined a 2013 model which uses an airfoil-airmass interaction model to investigate dual airfoils. The results showed that the power drop was significantly more in the dual airfoil but with more wing area it still extracted more power than the single airfoil. This is the first simulations using a twin airfoil. ³⁵

2015-2018

In 2015, Mechael Erhard and Hans Strauch developed a flight controller design which implements an accurate direction control toward target points, creating an eight-down flight pattern. This control system was then used on a fully automated pumping-cycle small scale prototype. Using a 30 m^2 kite linked to a 50 kW electrical motor and flying in 8 m/s winds. Mechael research is regarded as the first proof of concept without an optimized system of a pumping cycle aircraft. With the experimental results compared to Loyd's optimal conditions it shows that Loyd's predicts a power generation of 19.7 kW while the average power of the system yielded 3.5 kW or about 18% of the optimal power production. ³⁶

In 2015, Fechner further developed a dynamic power model by generating a point mass model and 4-point model. The tether was divided into a fixed number of lumped masses connected by springs and dashpots to provide more fluid structure analysis. The 4-point model was more accurate when determining dynamic effects of a kite control. ³⁷ In December 2016, Makani first generated electricity in crosswind flight using the M600 prototype. The kite design intended to produce up to 600 kilowatts, enough to power 300 homes. ¹²

In 2016, M. De Lellis et al. conducted an economic analysis of electrical power generation using pumping kites. They compared a 2 MW , 3 bladed wind turbines to pumping kite system for large scale power production. The cost analysis uses the internal rate of return as the economic

indicator to evaluate profitability. Using conservative cost estimates for the pumping kite system, analysis show that a pumping kite-based wind farm costs can be 74% of a conventional wind farm. By adding 13 pumping kite systems to existing wind farm with 21 wind turbines the internal rate of return doubles; furthermore, if the wind turbines were replaced with pumping kite units, the internal rate of return would triple. Pumping kites can also be more economically attractive in locations where wind turbines are not. These benefits largely come from lower transportation costs, and assembly costs. ^{16,38} Antonello Cherubini et al. explored the use of an AWES installed on a floating offshore platform using both a moored heaving platform coupled with the dynamic flight of a crosswind AWES to generate electrical energy. The results show that offshore AWES are theoretically viable and may be more efficient than grounded systems by taking advantage of harvested power from ocean waves. By simulating the configuration with 6 different aircrafts and see states the model can be used for iterative design process for offshore applications. ³⁹ Ivan Argatov and Valentine Shafranov evaluated the economic viability of small-scale AWES for off grid applications. Their study concludes that because tether drag, and cost, is proportional to the length, it is cheaper to have multiple smaller scale AWES rather than a larger scale system. Also, to make larger scale AWES economically feasible, reducing the cost of tether material and increasing the strength is necessary. The tether is one of the most important variables to reducing overall costs of AWES. ⁴⁰

In 2017, the first dynamic flight tests used to acquire time domain model-based parameters. These parameters were then used to generate a non-linear mathematical model. The results show using real flight tests is able to improve the predictive capability of low accuracy models however baseline models are equally important to deal with nonidentifiable dynamics and designing maneuvers for system identification. ¹⁰

One of the many difficult problems implementing AWES is the launching of a tethered rigid aircraft. L. Fagiano and S. Schnez conducted a feasibility analysis on four different launch systems, evaluating technical viability, economic viability, additional power required, and approximate ground area. The launch systems included 1) vertical take-off with rotors 2) Rotational take-off 3) linear take-off with on board propellers 4) winch launch. With linear take-off maneuver proving to be one of the most viable solutions while using propellers is costlier. The results do predict slightly higher larger on-board power values, but they are small compared to the total energy of the system while the take-off equipment constitutes a small cost fraction of the entire system. ⁴¹

2.2.2 Composite Structures and Design

Before 1900

The first modern development of fibers didn't occur until 1860 and 1879 which Joseph Swann and Thomas Edison creating the first carbon filaments. ⁴² This was quickly followed by Lewis Latimer who developed the first reliable carbon wire filament. ⁴³ These first filaments were very brittle and didn't have the structural properties of modern carbon fiber.

1900-1949

The beginning of modern composites is often attributed to Games Slayter in 1932. He accidentally created the first glass fibers by directing a jet of compressed air at a stream of molten glass. ⁴⁴ In 1937 Owen Corning Fiberglas Company began using the patented fiberglass technology and marketing it as wool or insulation but structural products soon followed. Using phenolics the first thermoset resin system, was created in the early 1900. With polyester patented by Carleton Ellis in 1936 and epoxies were invented in 1938. ⁴⁵ Structural composites were first used on fiberglass boats made in 1942, while Douglas Aircraft revolutionizing the mold fabrication market by using temporary phenolic/fiberglass molds. ⁴⁶ During world war 2, the

1940s marked the beginning of modern design and manufacturing techniques such as filament winding, chopped fiber, sandwich structures, and prepreg materials. In 1948 Eric Reissner, developed equations for plate buckling which include the effect of transverse shear stresses and further showed that the equations for buckling using linear theory decrease in accuracy as core's durometer decreases in accordance with the face sheets.⁴⁷ While the first honeycomb core was patented by Clare E. Bacon for the use in light weight structural panel construction.⁴⁸ As well as the development of impregnated fibers which Robert Steinman patented glass fibers impregnated with resin to be cured under heat and compression.⁴⁹

1950-1969

The next decade high performance fibers were created, and a manufacturing technique developed. In 1956 Roger Bacon discovered carbon vapor deposition. When Roger measured the mechanical properties of the fibers, he determined they had a modulus of 700 GPa and a tensile strength of 20 GPa. Roger Bacon published his work in 1958 and patented the method in 1960.⁴⁸ In 1964, Akio Shindo developed polyacrylonitrile (PAN) based carbon fibers. With a carbon fiber that contained 55%, carbon the fibers had sufficiently high modulus and strength to be used in reinforced composites.⁵⁰ In 1965, Boron fibers were also developed.⁴⁶ Boron fiber were quickly followed by pitch-based carbon fiber, in 1968, which had a carbon content of 85%. Due to the homogenous and smaller crystal structure the pitch-based carbon fibers prove to have higher modulus.⁵¹

1970-1979

In 1971, Stephen W. Tsai and Edward M. Wu published their failure theory for anisotropic materials. Their theory was ideal for use in developing composites because it takes into consideration difference in strengths due to positive and negative stresses, can account for different material symmetries, multi-dimensional space, and multi-axial stresses. Latter this

theory is known as Tsai Wu failure theory.⁵⁰ In 1972 W. T. Freeman and M. D. Campbell took measurements on five different composite systems containing high modulus graphite filaments with a negative coefficient of thermal expansion and three different resin systems. By measuring the longitudinal and transverse strain of the samples the hygrothermal effects are evaluated. It was shown that moisture content had a significant effect on thermal strain versus temperature hysteresis of both the resins and composites. The data showed that quasi-isotropic laminates of $0/\pm 45/90$ and $0/\pm 60$ exhibit low expansion coefficients over a 355 °C temperature range.⁵² In 1976, R. Byron et al. determined the classical diffusion equation and obtained yielding moisture profiles through the laminate. These equations were physically tested using T300/5298 graphite-epoxy and showed that the magnitude and distribution of hygrothermally induced stresses through the laminate.⁵² The Beech Starship was created in 1978. With high specific stiffness and strength composites used, the aircraft was the first fully filament wound aircraft fuselage for civilians. The aircraft had extensive use of carbon fiber and was certified by the FAA.⁵³

1980-1989

During the late 1970, and early 1980, the development of nondestructive testing occurred and increased use of high modulus fibers were applied in aerospace, automotive, marine, energy, infrastructure, armor biomedical and recreational applications. Throughout the 1980, a variety of patents were submitted in regard to composite turbine blades for a wind turbine. In 1980 and 1981, United Technologies patented two similar designs of filament winding a simple composite wind turbine blade that could be helically wound in a single pass. The purpose of this system is to develop light weight single piece wind turbine blades.^{54,55}

This development was followed by a patent from DWR Wind Tech Inc, who developed a wind turbine blade that increases power production at lower Reynolds numbers, reduce turbine loads

from off axis winds, and maintaining low manufacturing costs. The rotor has an outer skin of fiberglass mat impregnated with a polymer resin. ⁵⁶

1990-present

Although carbon nanotubes were first discovered in 1952, published in a Soviet Journal. In 1991, Sumio Iijima is credited with the recent advancement and interests in the needle like carbon structure. Electron microscopy showed each needle comprises of coaxial tubes of graphite sheets ranging from 2 to 50. The microstructure of the tubes consists of carbon atom hexagons arranged in a helical fashion about the needle axis. ⁵⁷ With the variety of applications carbon nanotubes brought there was thought that they will be the next high-end fiber. In 1999, J. P Sivetat et al. carried out the first mechanical measurement on single walled carbon nanotubes. The results show that carbon nanotubes have a Young's Modulus at least as high as graphite and higher for small single walled nanotubes. The correlation between order and strength is stated as critical for their application in composites. It has been also shown that good load transfer between polymer matrices and the outer surface of carbon nanotubes show that they should excel in Composite application. ⁵⁸

2.2.3 Additive Manufacturing

1980-1989

Additive manufacturing first began in the 1980's as rapid prototyping technique. In 1981, Hideo Kodama created the first stereolithography additive manufacturing system using a photo hardening polymer when exposed to ultraviolet rays. Two of the systems used masks to generate the pattern for that plane while the others used a scanning laser. It was shown that using the selective laser would give higher resolution depending on the diameter of the beam however would take considerably more time than the masked system. ⁵⁹ In 1986 this technology was first

patented by Jean-Claude Andre et al., while Chuck Fall, in the United States was also patenting a similar system. ⁶⁰ However, Hull's development of Standard Tessellation Language, or STL, allowed for the digital slicing of 3D models into small triangles or a coordinate triplet. Even though the file format is inaccurate, it allowed for modern infill strategies to be developed. ⁶¹

1990-1999

The 1990's saw the addition of many new systems to the market such as Fusion Deposition Modeling, Ink Jet Printing, Laminated Object Manufacturing, and Selective Laser Sintering. The most common additive manufacturing technique used by hobbyists, Fusion Deposition Modeling or FDM, was developed in 1988 and patented in 1992 by Steven Scott Crump. Scott's patent stated that it could be used with any material which could bond to the previous layers of the system. ⁶² However, the first materials used in 1991 were casting wax, wax-filled plastic adhesive material, and nylon. Nylon was quickly replaced with Acrylonitrile Butadiene Styrene (ABS) and other elastomers in 1994. At this time experiments were conducted on extruding low melting point alloys however, there were issues due to the low viscosity and surface tension of metal. ⁶³ In 1993, the term 3D printing was coined by MIT's development of a powder passed inkjet printer. Using either powdered ceramic, metal, or the combination of the two to create complex composite parts. The inkjet system proved to be one of fastest additive manufacturing techniques. ⁶⁴ In 1996, Bayersches Laser Zentrum, created the first Selective Laser Sintering (SLS) system, using a high central beam for sintering and a low-density beam for preheating the powder. This process was able to print a diversity of materials ranging from plastics, metals, and a combination of metals and ceramics. ⁶⁵

2000-2009

For a long time, the combination of 3D printing and reinforced fiber have been discussed; however, the fabricating useful parts has proven difficult due to the low interfacial bonding

strength. Stereolithography (SL) initially proved to be the most promising in terms of incorporating fiber reinforced 3D printed structures. Some of the first fibers were incorporated into 3D printed parts in 2000's but the mechanical properties still lacked.⁶⁶

The application of 3D printing has been quickly adopted industry, especially with the increase in accuracy, and begun to make final products while initially it was developed to help visualize and prototype products. The versatility of using a variety of materials was shown in 2003 with the development of a cellular jet fusion-based printer, developed to create organs. It was determined that organ printing is a feasible method and has the possibilities of increasing the ability to screen assays for drug discovery and testing while also providing other applications in biomedical research. The development of the first organ 3D printer spurred a variety of different research and systems for medical application.⁶⁷ Nylon has been a common polymer used in the development of 3D printers. Nylon 6 was first used but Nylon 12 (PA 12) was less commonly used until 2001 when an SLS system was patented.⁶⁸

In 2005, as SLS was being further developed the two developing technologies of SLS and carbon nanotubes were combined. The carbon nanotubes were added to the polymer through melt blending using a twin-screw extrusion then the polymer is chopped into 50 microns pellets. The carbon nanotubes changed the thermal properties of the powder resulting in the material being overheated, confirmed by DSC testing. Also, significant porosity was observed using SEM images, significantly reducing the strength of the material. Overall this resulted in materials that were lower strength than injection molded parts.⁶⁸

A study was conducted on different SLS systems in 2006 by Zarringhalam et al. Using multiple blends of PA 12 the quality of the final 3D printed parts were determined using optical, crystalline, thermal and mechanical properties. Results showed that increased temperature increased the molecular weight substantially, and that the mechanical properties of the SLS parts were similar to injection molding. However, the presence of unmolten particles resulted in a composite like structure with a variety of boundaries and interfaces effecting the mechanical properties. The mechanical properties of the PA12 were comparable to injection molding; however, the max strain was an order of magnitude lower than that of injection molded parts. The DSC showed melting points peaks of 189 °C which is an 3 °C higher than previous PA 12 used in SLS systems. Showing parts continued to be adversely affected by uncured particles. ⁶⁹

2010-2018

Fused deposition modeling (FDM) gained increasing popularity due to its low cost minimal by product, and adaptive material change. In 2015, Fuda Ning was the first to add carbon fibers to the feed stock of an FDM printer to adjust the mechanical properties. He used ABS and mixed with two different length carbon fibers, 100 μm and 150 μm with a common diameter of 7.2 μm . Using different concentrations of fiber to polymer a plastic extruder extruded 2.85 mm filament to generate the parts. The results showed an initial increase in tensile strength; however, if the carbon content increased more than 7.5 wt%, a sharp reduction in tensile strength occurred. The largest mean tensile strength was found at 42 MPa for the 5 wt% while the lowest was 34 MPa for 10 wt%. A similar trend was observed with Young's Modulus with the largest Young's Modulus at 2.5 GPa at 7.5 wt% carbon content. When comparing the two length fibers, the longer fiber, 150 μm , had the largest tensile strength and young's modulus while the 100 μm fiber had the better toughness and ductility. The flexural stress also increases 11.82%,

while the flexural modulus 16.82%, and the flexural toughness 21.86%. Showing that the fiber reinforcing can considerable improve the mechanical properties of 3D FDM prints. ⁷⁰

In May 2016, HP revealed their first production ready 3D printer system using their multi jet fusion technology; the printer was similar to the first system developed by MIT. In February 2018, HP revealed one of the first fully colored 3D printing systems using the same technology with advances in their fusing agent. The first model used powdered PA12 in the bed then a black fusing agent is applied via their multi jet fusion technology. The black fusing agent absorbed high amounts of infrared light allowing the particles to heat up and be sintered together. HP's initial system revealed in 2016 is the primary system used for the research in this paper. The most recent system which can print in color is a result of HP clear fusing agent that can still absorb infrared light and fuse the PA12 particles. HP's method only uses the clear agent on the exterior of the printed part as a new black fusing agent is used in the center. ⁷¹

2.2.4 Hybrid Manufacturing

2000-2009

Stereolithography (SL) initially proved to be the most promising in terms of incorporating long fibers in reinforce 3D printed structures. ⁶⁶ In 2003, a study conducted by Karalekas studied two different photo curable resin systems, an epoxy based, and an acrylic based one, while adding three different fibers E-glass, PAN based carbon fibers, and Aramid fiber mat. The printing process was stopped mid-way through to add the fibers to the 3D printed structure. The results showed an increase in elastic modulus and maximum strength with a significant reduction in the strain of the material. The E-glass performed the best with its tensile strength improving 48%

and strain to fracture decreasing by 51%. These tests was the first proof of concept of long fiber reinforced 3D printed parts as there were processing issues. ⁷²

In 2004, Gupta et al. attempted a dual cure system because the general matrix didn't successfully cure with the exposure to UV rays. The uncured resin resulted in surface tackiness, and lower structural strength. Using Differential Scanning Calorimetry (DSC), it was estimated that a quarter of the resin remains trapped inside the carbon fiber tow. Using a thermal curing step proved to cure the remaining resin within the tows. The average tensile strength of samples without the post cure was 46.9 ± 9.4 MPa while the cured samples were 61.3 ± 10.3 MPa, showing an increase in tensile strength after the post cure. ⁷³

2010-2018

The year 2016 marked the development of a long fiber 3D printing methods. The goal of the first system developed by Nanya Li et al. was to use bio polymers, specifically Polylactic acid (PLA). The carbon had weak interface bonding between the carbon fiber and PLA thus a sizing agent was used to improve the interfacial bonding. The carbon used was a tow of 1000 fibers with 98% pure PLA with a fiber to polymer ratio was 34%. The 3D printer prototype used an FDM style extrusion with the printer head heating the PLA, turning it molten and adding the continuous fiber. The fiber and polymer are extruded together like an FDM printer. The sizing was applied to the fiber before the printing process using dissolved PLA particles and high-speed shear emulsification. Next, ionized water and the carbon fibers are added to the solution to process the PLA sizing agent which modifies the surface of the carbon fibers. Three different samples of PLA, carbon fiber reinforced PLA, and carbon fiber with sizing agent reinforced PLA were tested using tensile strength, flexural strength, and dynamic mechanical analysis (DMA). For the tensile test and flexural strength of the three systems the sized carbon was the strongest with a

tensile strength of 91 MPa and flexural strength 156 MPa. The unprocessed carbon fibers outperformed the PLA in tensile it was 80 MPa while the PLA was 28 MPa and the flexural was 59 MPa with the PLA being 53 MPa. These reinforced PLA showed better mechanical properties than chopped fiber reinforced filament used in FDM printing, which had a maximum value of 68 MPa compared to the 91 MPa of the sized carbon used. An increase of 164% was achieved with the addition of sized carbon which showing the importance of the interfacial bonding. SEM micrographs, dynamic modulus and glass transition temperature (T_g) show the lack of void content and better interfacial bonding between the PLA and fibers within the system and resulted in less fiber pullout at the fractured surface with higher storage modulus and T_g than the other two samples.⁷⁴

Xinhua Yao et al. used a similar technique to Karalekas study when trying to determine the health of stereolithography parts by measuring the resistance of the carbon fiber. The process allowed the printer to print half way through one of its cycles, then the impregnated fibers are added manually to the 3D printed part. A tensile test and 3-point bend test were used to determine the tensile and flexural properties of the hybrid parts. A dynamometer was used to preload the fibers with 2 Newtons. 3 types of Toray fibers were tested with the method all PAN bases T300, T700 6K, and T700 12K. Similar to Nanya Li et al. the fibers were impregnated with a PLA adhesive, a two-part epoxy adhesive in to increase the interfacial strength between the fibers and PLA. The tensile tests using T300, T700 6K, and T700 12K showed increases in the tensile strength by 36.8%, 58.86% and 70.02%. The system allowed for an increase in strength of the final product while also reducing the print time and final weight. Similar results were shown for the flexural tests; however, it only improved around 4.6% when comparing strength to weight ratio. It was also viewed that there was delamination between fibers and PLA

showing poor interfacial bonding, similar to Nanya Li et al. Xinhua Yao et al. also studied the gauge factor or the piezoresistive effects due to the applied loads in the carbon fiber to try and correlate strain and stress to the resistance of the fiber. The measurements of the piezoresistive were repeatable and were accurate although it's believed that there was significant debonding of the fiber from the polymer resulting in less accurate results. ^{74,75}

Tiantian Li and Lifeng Wang also conducted experiments, in 2017, on 3 different 3D printed sandwich core structures. The printed geometries were truss, conventional honeycomb, and re-entrant honeycomb. These geometries are used to further tailor the bending properties and failure mechanisms of the composite sandwich panel. A finite element model using Abaqus was created to compare the results. The honey comb and re-entrant honeycomb structure are orthotropic and have a full infill in order to have a large surface area for the composite material to interface with the core. The core material is VeroWhite which is an acrylic based polymer. The composite face sheets layup schedule was also $(0^\circ/90^\circ)_4$ for a total of 16 plies. They show that the topology has significant impact on the load and deflection curves. The truss sandwich core had the largest flexural stiffness and maximum loading forces while the reentrant honey comb had the lowest flexural stiffness and largest bending deflection. The re-entrant honey comb has an auxetic behavior to the bending load while the truss system and regular honey comb have a non-auxetic behavior. It was shown that the re-entrant honeycomb had significantly higher energy absorption due to sequential breaking of instabilities where the honeycomb and truss system show catastrophic failure due to a stress concentration. Using 3D printing parts as a core structure can further tailor sandwich panels to improve their energy absorption and ultimate load. ⁷⁶ Wenfeng et al. fabricated a 3D printing platform similar to FDM, which had significant limitations when manufacturing complex geometries. The system used a

fiber bundle, epoxy pool, control system, building platform, X-Y motion mechanics, printer head, and conveying pipe. The system was limited as it couldn't fabricate a scaffold, severely limiting its vertical printing ability. The tensile strength of the continuous fiber was stronger than long fiber reinforced thermoplastics and short fiber thermoplastics of previous studies. However, there is large variability between prints showing low reliability of printing system. The final tensile strength of the reinforced thermoset was 792.8 MPa, with an elastic modulus of 161.4 GPa in addition to the flexural strength being 202 MPa and the flexural modulus being 143.9 GPa.⁷⁷

3. Performance of a tethered Airborne Wind Energy System

With the diversity of AWES, it is critical to develop new models to represent aircraft control. This portion of the thesis focuses on the numerical model and the wind tunnel study, allowing for rapid adjustments to aircraft design and accounting for new models that have not been previously into considered.

3.1 Numerical model

The numerical model is comprised of the following three sub-functions: Tornado, power generation model, and flight characteristics. The numerical model is a program written in MATLAB that allows the geometry of the aircraft to be generated, defined flight capabilities, and a model for extracted power from specific environmental conditions. The first sub function, Tornado, allows the geometry and the wind speed to be rapidly defined. Tornado also uses the defined geometry and Vortex Lattice Method (VLM) to determine basic aerodynamic coefficients of the aircraft. Angle of attack sweeps are used to evaluate the coefficient of lift, drag and the aircrafts moment coefficients. The aerodynamic coefficients and flight orientation

are then used as inputs for the power generation model. The power generation model uses the point mass method to determine the loads of the aircraft through a specified flight path. These loads are then translated into tether tension, which is converted to power through a generator. The aerodynamic loads are combined with a pitch stability model with a new derivation to determine how the tether affects the stability of the aircraft. The theory and results produced by the numerical model will be discussed further in the next three sections.

3.1.1 Tornado (Vortex Lattice Method)

Tornado uses the Vortex Lattice Method (VLM) to analyze linear aerodynamics pertaining to aircrafts. Written in MATLAB, Tornado is an open source program developed by Tomas Melin of the Royal Institute of Technology for use in the conceptual design phase of an aircraft. The theoretical basis of Tornado is VLM. Since VLM is one of the original computational fluid dynamic methods, it is a well proven technique. Using MATLAB as the program language allows the code to be modified and implemented into other programs, as a sub function which is the approach utilized for this research. With the ability to support multi wing designs, a variety airfoil cross sections, and wing configurations such as swept, tapered, cambered, twisted and cranked wings with or without dihedral, the program allows for a large degree of geometric flexibility. In addition, the inclusion of control surfaces such as canards, flaps, ailerons, elevators, and rudders, enables the effects of control surfaces on the aircraft to be determined. Defining the geometry, orientation, and configuration as well as the flight conditions make the program ideal for deriving the aerodynamic coefficients of the airfoil and control surfaces. Using VLM as the theoretical basis allows for a complicated analysis to be done efficiently.⁷⁸

VLM was developed in 1910, by L.F. Richardson, to obtain numerical solutions by using the integral of the loading that relates the normal velocity and wing loading. In the 1970's, many

different fluid dynamics questions were analyzed with various modifications, such as: wing aerodynamics and component interaction, subsonic finite element for wing body combinations, modeling lifting surfaces with thickness, induced drag or optimum loading for non-planar aircraft, and optimization and design of 3D aerodynamic configurations. VLM has been primarily used for the analysis of wings with its ease of parameterization. The theory behind VLM has increased in complexity especially with the additional computational power of computers.⁷⁹

VLM stems from potential flow theory, where flow is modeled with a combination of potential lines and streamlines. The aircraft is modeled by solving linear partial differential equations, often Laplace equations. This results in the important conclusion that any solution of a Laplace equation represents the stream, meaning that a complicated flow pattern for irrotational, incompressible flow can be modeled by adding together a series of elementary flows. These elementary flows are uniform flow, source flow, sink flow, and vortex flow. VLM is based off the assumption that the inviscid velocity field of the air around the aircraft can be modeled using a distribution of discrete vortex segments. The solver is not sensitive to the type of fluid as viscosity is negated; however, fluid density does affect the results. In the case of aerodynamics, the density is that of air. By simulating the flow field around the aircraft, one can achieve a force distribution around the simulated body that is equivalent to the pressure distribution on the surfaces. Though the VLM cannot compute viscous, drag the induced drag from creating lift of the aircraft can be estimated.

VLM models can be solved in a variety of ways, but they are based on the theory that the flow field is modeled using the superposition of straight vortex elements. The forces can be computed

by applying the boundary condition that the surface is impermeable to tangential flow and then breaking the aircraft geometry into a lattice structure of vortices. The strength of the vortices can then be used to calculate the resulting loads for each lattice segment.

The geometric surface is segmented into a lattice structure and panels, as in other finite differencing methods such as Finite Element Analysis (FEA). Once segmented, each panel is modeled as a two-dimensional surface, even if the surface is 3D, by requiring that the surface is infinitely thin. Each panel's flow manipulation is then modeled by apply a horseshoe vortex to each panel that consists of three same sized vortex elements and a collocation point. The collocation point is the location where the impermeability boundary condition is satisfied. Using the collocation point and the horseshoe vortex, an influence matrix is generated by using the distance of the collocation point to each vortex creating the system of equations. The system of equations to be solved is then the vortex strengths based free stream velocity, influence matrix, and projection of the free stream normal to the surface. According to Kutta Joukowski's theorem, the lift acting on each panel is shown below as a function of air density ρ , free stream velocity V , length of the cross-span vortex l and, vortex strength Γ ⁸⁰.

$$L = \rho V \Gamma l$$

As shown in the equation above, the lift is the cross product of the local velocity and the span-wise vortex vector. To calculate the induced drag, another influence matrix needs to be computed. Once these loads and pressure distributions are determined, a system of equations is used to determine the aerodynamic coefficients. Coefficient of lift is defined by summing all the forces perpendicular to the free stream F_{\perp} , which equates to the local lift in the symmetry plane. With all the loads divided by the dynamic pressure q and the wing surface area S , the unitless force component perpendicular to the free stream is calculated.

$$C_L = \frac{\sum F_{\perp} \bar{v}_{\infty}}{qS}$$

The coefficient of drag is equally as important as the coefficient of lift in aircraft design.

Composed of many different factors, VLM doesn't consider viscous effects, nor the effects of thickness, but it does evaluate the induced drag C_{D_i} . Induced drag can contribute to 40% of the total drag during cruise flight and 80% during landing configurations ⁸¹. The equation is similar to coefficient of drag but is the unitless force component parallel to the free stream F_{\parallel} .

$$C_{D_i} = \frac{\sum F_{\parallel} \bar{v}_{\infty}}{qS}$$

Because VLM only models induced drag, the following equation can be used to model the total drag of the aircraft.

$$C_D = C_{D_o} + \frac{C_L^2}{\pi AR}$$

The wing profile drag coefficient C_{D_o} is defined as to a wing drag with a infinite aspect ratio and depend only on the airfoil section of the wing. Where, $\frac{C_L^2}{\pi AR}$ refers to the induced drag of the

wing. The other variables are the coefficient of lift C_L and the aspect ratio of the airfoil AR ^{82,83}.

Using these values many of the performance characteristics of the aircraft can be defined such as the glide slope, span load, and lift slope. Glide slope is the slope of the glide polar with the largest value glide slope resulting in the angle of attack with maximum lift for the least amount of drag. The lift slope, when compared to angle of attack, is linear before the airfoil stalls.

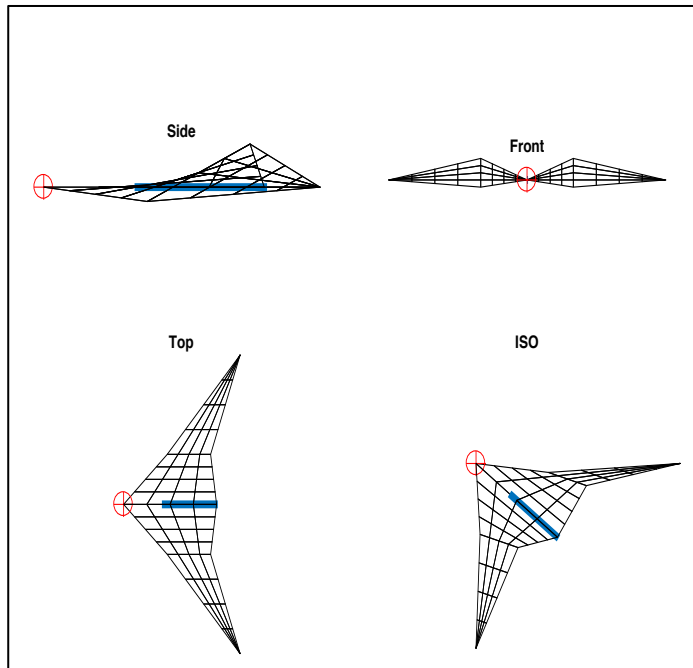
Compared with the wing loading and maximum angle of attack the max coefficient of lift can be determined, an important design characteristic.

When in the conceptual and preliminary design steps of designing an aircraft, it is not worth the time to utilize complex nonlinear CFD models because one will only be able to analyze and design a few geometries over a long period of time. While VLM is a quick process and provides accurate loads in linear region of flight before stall. The simplified model allows for a high degree of geometric flexibility and quick computational time, making it ideal for the purpose of designing and testing a variety of geometries. VLM gives the ability to design aircrafts with multiple wings, complex geometries, and control surfaces and also to obtain the aircrafts 3D forces, aerodynamic coefficients, and stability derivatives with respect to angle of attack, sideslip angular rates and rudder deflections. This makes VLM ideal for the conceptual and preliminary design of an aircraft, while nonlinear models should be utilized for the detailed design and development of the aircraft at the same time as physical testing.

Tornado uses specific inputs to define aircraft geometry and test state which VLM then uses to solve the aerodynamic coefficients of the aircraft. Written in MATLAB, the program is a 3D-vortex lattice program with a flexible wake. Flexible wake means the vortices evaluated on the leading wing element can affect flow further downstream on a secondary wing element providing information on wing wash. Tornado is broken down in to a couple sequential process:

- 1) Define the geometry of the aircraft
- 2) Define flight conditions and orientation of the aircraft or type of sweep
- 3) Define the processor and outputted results
- 4) Post process and analyze results.

The geometry is defined by the following variables with a wing being able to be partitioned multiple segments. The aircrafts configuration can then be saved and loaded for use in different states and configurations. The geometry is defined using the required inputs for each wing partition, as listed below and shown in Figure 3.1:



- Apex coordinates
- Span
- Taper
- Sweep
- Camber
- Dihedral
- Twist
- Symmetry
- Root chord
- Flaps
- Flap symmetry
- Flap deflection
- Flap chord in as percentage of root chord
- Number of panels in chord direction (X)
- Number of panels in span direction (Y)
- Number of panels on the flap
- Root chord airfoil
- Outboard airfoil

Figure 3.1: Delta wing configuration and geometric variables.

The geometric inputs are critical for defining the geometry; for more complex wing geometries, semi span partitions are used. The delta wing configuration uses two semi span partitions to acquire its final wing shape geometry. Understanding of the location of the Apex coordinates is critical, as this defines the center of gravity and reference coordinate. For applications in this research, the center of gravity is assumed to be at quarter chord. First proposed by Italian Pistolesi and a rule used by Prandtl's lifting theory for VLM codes, the span wise vortex segment should cross the panel at quarter chord. Motivated from thin airfoil theory, the quarter chord allows both the lifting and pitching moment of a flat plate to be calculated, allowing that point to be the location where pitching moment is independent of angle of attack. Also, when defining the main element, you want to set the center of gravity and reference point to X to -0.25 while the Y and Z remain zero. Setting up this reference ensures moments and aerodynamic values are estimated properly. These values are used to create a 3D representation of the vehicle with any number of wings including a tail surfaces, and can even be used to represent winglets, and engine mounts. Partitioning of the geometry into the panels also happens in during this preprocessor

which different panel distributions can be applied to aid in the convergence of the solution. Linear distribution of the panels results in the slowest convergence as with span-wise cosine spacing yields faster lift convergence and resolves changing pressure coefficient at the leading edge with higher resolution ⁸⁴. Cosine spacing can also be applied in the chordwise direction for further improvements on lift convergence. Additionally, inserting a strip of quarter panels width at the wing tip, not meshed, reduced the error of the lift slope from 4% to 0.5% ⁸⁵.

Once the aircraft geometry is defined, the aerodynamic state can be defined. The following parameters are used to define the aircrafts orientation and free flow: Angle of attack, Angle of sideslip, Angular roll rate, Angular pitch rate, Angular yaw rate, Air speed. For simple analysis and processing these are used to define the flight conditions, aircraft orientation which can then be used to evaluate the basic dynamic effects of the aircraft. Once the geometry and flight conditions are defined in 3D, VLM can be applied to derive the solution.

Tornado's processor has a couple of different methods regarding simulations. It allows a simple solution for an aircraft which takes the pre-defined aerodynamic state and evaluates the aerodynamic coefficients for that configuration. Other simulations allow sweeps of orientation the aircraft for angle of attack (Alpha), yaw (Beta), and roll (Delta). VLM then solves for each scenario, sweeps take a significant longer period of time as it's assessing different flows for every angular configuration which significantly increases the time. The values from VLM are then postprocessed providing a variety of data. This research is focused on the aerodynamic properties especially through the angle of attack range, as the coefficient of lift and drag is important for improving the efficiency of the AWES.

This code was further modified to interface directly with subsequent sub programs to analyze the power output, performance characteristics, to provide valuable information on that configuration, and compare directly to others with the ability to scale and understand what affects by using unitless numbers.

Two geometries were studied further using these analysis methods shown in Figure 3.2 and Figure 3.3. A convergence study was applied to the geometries to make sure there was little discretization error for the simulations. Figure 3.2 shows the geometry of an ASK 21 German glider while Figure 3.3 shows the stunt kite geometry.

The ASK 21 is a popular German glider designed by Rudolf Kaiser. Primarily used for training new gliders it also can be used for cross country flights and aerobatic instruction. Using a thick wing profile, T tail, and large aspect ratio, the glider is very efficient. It possesses the ability to climb using weak thermals and very good pitch stability. These characteristics are extremely appealing especially the high lift to drag ratio is expected to generate the most power when used as an AWES. ⁸⁶

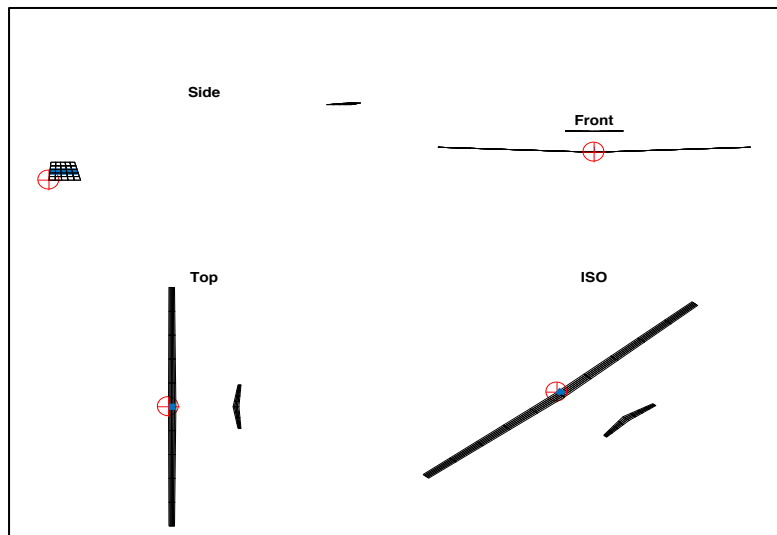


Figure 3.2: ASK 21 glider geometry.

The second geometry configuration uses a delta wing configuration commonly used for stunt kite geometries. With very tight turn radius and high degree of agility it can be ideal in take-off and landing situations. Takeoff and landing for AWES have provided significant issues in modern development of the systems. This delta wing configuration is also wind tunnel tested to analyze its high angle of attack aerodynamic coefficients.

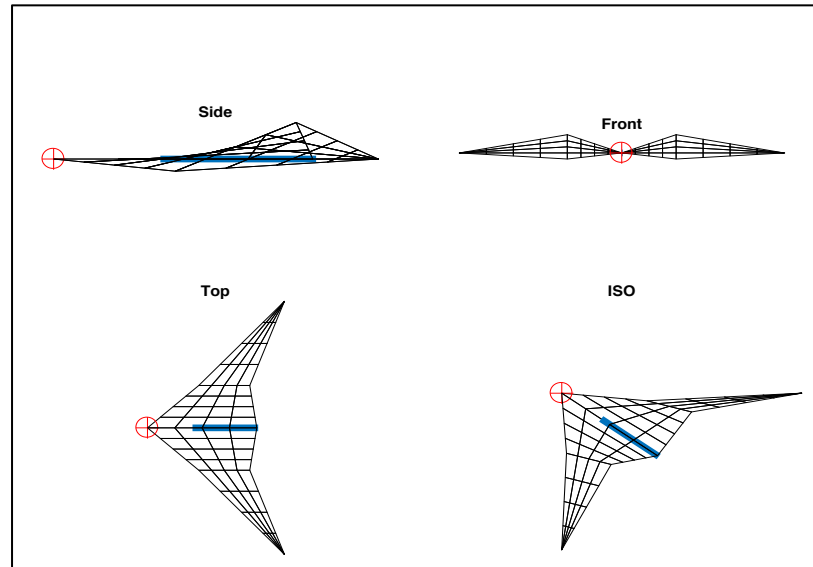


Figure 3.3: Delta wing geometry.

VLM is used to derive unitless aerodynamic efficiently once the geometry is defined, which would not be possible with nonlinear CFD models. In order for the physical geometry to be represented correctly the lattice structure needs to be sufficiently dense otherwise there will be discretization error. Discretization error is the difference between the mathematical model and the discretized model commonly used in Finite Element models. For this reason, a convergence study is conducted to make sure the model is correctly modeled, and the computation time isn't increased. Once the geometries and the lattice structure are defined the Vortex lattice method is applied and further processed into the aerodynamic coefficients, as described earlier.

A convergence study was applied to reduce the discretization error while minimizing computational time. The convergence study was conducted on the coefficient of lift and drag by increasing the mesh density by the element order. As shown below, the models for lift converged more quickly than the drag. The geometries converged close to the same element density. The coefficient of lift converges around a mesh density of four elements to model a wing where the induced coefficient of drag didn't converge until 32 elements with a computational time of 15 seconds.

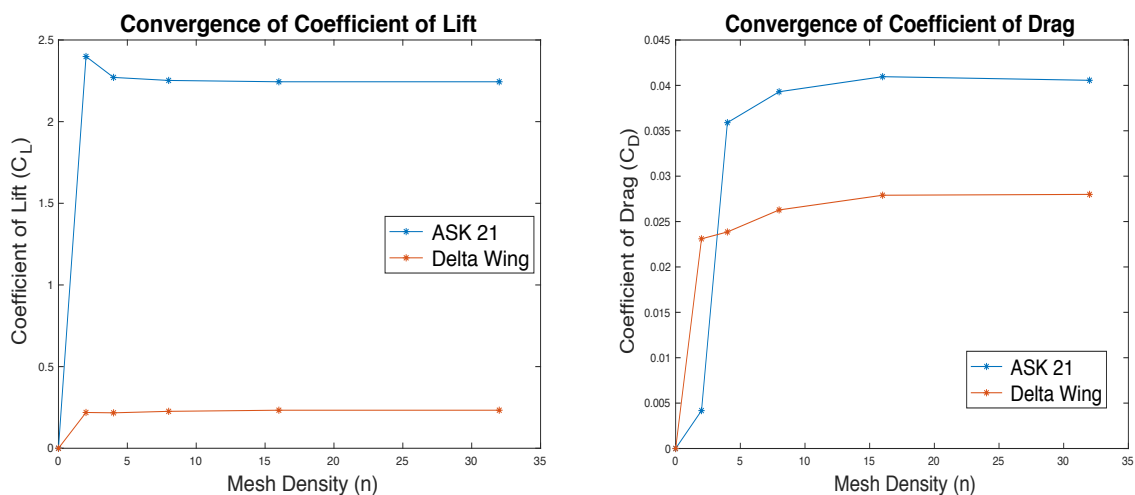


Figure 3.4: Convergence study of the coefficient of lift and drag for the increased mesh density.

The VLM results were compared, showing that the ASK 21 geometry had a significantly higher C_L/C_{Di} ratio through the angles of attack.

The converged VLM output was compared with the experimental results within the linear region of the wind tunnel tests. Angle of attack was varied between -2° and 27° at Reynolds number (Re) of 48000, 73000, 9700, and 121000, presented in the wind tunnel segment. As expected, the Re has a larger effect on lift than on drag especially at stall. The reduced C_L values of VLM are the result of modeling slight differences in the geometry of the two models. The VLM model is incapable of modeling triangular anhedral and dihedral interface resulting in slightly different

longitudinal angle. Using a linear fit, the slope of the two data sets were 0.71 and 0.63. The 11% error can be attributed to the turbulent flow seen near stall. Ultimately, theoretical data was in good agreement with experimental data; thus, the panel code was used to estimate aerodynamic coefficients in different flight conditions up to 27° which is where separation of the flow, or stall, occurs. VLM doesn't model turbulent flow making the model inaccurate after stall.

3.1.2 Power Generation Model

With many other power models preceding this current model is used to rapidly evaluate tether tension using static aerodynamic coefficients through the cycle of its flight. The power generation model uses a variety of concepts derived from other models for determining the power density of AWES. With the first power generation model generated by Myles Loyd for crosswind energy generation more advanced models have been derived especially ones that take moment of inertia into consideration. The power generation model uses point mass method to fly a pre-defined flight pattern to determine aerodynamic loads, based on the static flight conditions of the aircraft. Once the load vectors are computed the time it takes to fly to the next point is determined, providing a time scale for the total cycle. Using the aerodynamic loads and the assumption that the aircraft translates radially at a constant speed the tether tension can be evaluated. Through the time scale and understanding of the tether tension throughout the cycle the power can be evaluated compared to the energy it takes to bring the cycle back to its beginning condition. This model is similar to Fchener and Schmehl model which doesn't consider dynamic effects nor unpredictable environmental conditions such as gusts. Fchner and Schmehl's model is broken up into two process to represent the pumping cycle: 1) the energy generation cycle 2) the reel in cycle. The energy generation cycle represents when the tether is being drawn out while the aircraft is flying the specified flight path. The reel in cycle is the

process brings the aircraft back to its initial condition. The aircraft is stalled which allows it to be reeled in using a small percentage of the energy the aircraft generated.

The inputs for the power generation are can be broken down into four different groups based on what they characterize. These four areas are, aircraft characteristics, environment, flight path, and tether data. VLM outputs, as discussed earlier, output the aerodynamic coefficients such as coefficient of lift, and coefficient of drag for a series of different angle of attacks. These unitless coefficients combined with the physical characteristics of the aircraft such as the wing area and mass aircraft fully define the aircraft to be used in this model. A pre-determined flight path and max height is inputted into the code to define the power generation phase, other flight paths can be used, however the maximum loading of tether occurs when using a cross wind figure eight flight pattern.²⁶ The maximum height is also inputted to signal the end the power generation phase and begin the real in phase for the code. The last inputs are a tether data base which the code can draw from. The tether needs to be able to handle the max loads of the aircraft generates and the geometry of the tether significantly affects the drag of the system. The code choses the geometry and material of the tether based on the max loads seen by the aircraft. These inputs are used to determine the loads generated converting them to tether tension, through a series of functions, which can then be related to the total power generated for the system.

The solving processes uses the inputs and solves the loading condition for each point mass location in the flight path using the aerodynamic coefficients and apparent air speed. The program is based off of Shmehl, Noom, and Vlugt's model which uses a steady state model using polar coordinates to define the aircraft and flight path. The bulk of the main code solves a loop for each point of the flight path calculating loads, velocity, apparent wind and translating them into tether tension to estimate the power output. The first step of the function is determining the

aircraft's configuration for it to attain the next point of the flight path. The forces generated by a flying wing are denoted as the sum of the lift (L) and drag (D) vector with the magnitude calculated using the following equations:

$$L = \frac{1}{2} \rho C_L v_a^2 S$$

$$D = \frac{1}{2} \rho C_D v_a^2 S$$

Where C_L and C_D are aerodynamic lift and drag coefficients, ρ is the air density and S is the surface area. The apparent wind (v_a) is defined as the local air speed the aircraft sees and is the sum of the aircraft's velocity and wind velocity vectors. With this basic understanding, aerodynamic loads can be converted into tether loads. These loads then act through a single point on the wing and are approximated through a sequence of steady state changes. A characteristic feature of a light weight traction wing is that the aerodynamic forces and tether force are the dominate forces within the system.

Three assumptions are used for this model. Assumption one: there is no acceleration through the tether axis, meaning that during the power generation phase and reel in phase the tether is being drawn in and out at a constant rate. Assumption two: the tether is connected to the center of the gravity aircraft, meaning that it doesn't affect the controls or orientation of the aircraft.

Assumption three: the aircraft has the control authority to fly the pre-determined flight path.

Since the aircraft operates using a variable length tether attached to a ground-based generator the motion of the wing can be defined using two fundamental components. The component along the tether which is controlled by the ground station and the component perpendicular to the tether controlled by the flight control system. For this reason, a spherical coordinate system is used to

define the kinematic analysis of the aircraft with the origin located at the ground station. The following transformation matrix allows the apparent wind to be defined in polar coordinates:

$$v_a = \begin{bmatrix} \sin \theta \cos \phi \\ \cos \theta \sin \phi \\ -\sin \phi \end{bmatrix} v_w - \begin{bmatrix} 1 \\ 0 \\ 0 \end{bmatrix} v_{k,r} - \begin{bmatrix} 0 \\ \cos \chi \\ \sin \chi \end{bmatrix} v_{k,t}$$

Using spherical coordinates (r, θ, ϕ) and the course angle (χ) , measured in the tangential plane to the tether is the unit vector for the for the velocity of the kite. Summing the velocity vectors evaluates the apparent wind of the in the aircraft plane. With v_w magnitude of the wind, $v_{k,r}$ the radial velocity of the kite, and $v_{k,t}$ the tangential velocity of the kite. With the earlier assumption that there is no acceleration in the radial direction, it can be assumed that $v_{k,r}$ the radial velocity of the kite is equal to the velocity the kite is either being let out or drawn back in. Additionally, the tether needs to be able to withstand the aerodynamic loads applied to it with a safety factor of two. The max load of the tether can be defined as which is also used as the book result for tether tension based on the apparent velocity:

$$F_{T,max} = \frac{1}{2} \rho v_a^2 A_p C_D \sqrt{1 + \left(\frac{L}{D}\right)^2}$$

Which is dependent on the total drag of the system including the effective drag of the tether shown below.

$$C_D = C_D^k + C_{D,eff}^t$$

The effective coefficient of drag for the tether defined as is:

$$C_{D,eff}^t \approx 0.31 \bar{l} \frac{d}{A_p} C_D^t$$

The upper end of the tether is moving at the speed of the kite while the bottom is fixed. The relationship is dependent on the C_D^t the coefficient of drag of the tether perpendicular to the flow,

d the tether diameter, A_p projected area of the kite, and \bar{l} current length of the tether. The coefficient of drag of kite is determined through the VLM. Using a predetermined diameter and an estimated max apparent velocity the max tether tension can be estimated which needs to be less than the breaking force ($F_{t,b}$) of the tether divided by the safety factor.

$$F_{t,max} \leq \frac{F_{t,b}}{S_t}$$

The factor of safety used is two, as is common for consumer and industrial applications.

These equations created the basis for the code and understanding and the loads applied to the aircraft using spherical coordinate system. As stated earlier the flight path of the aircraft is the figure eight pattern projected onto a sphere with the origin at zero. The lift is then calculated based on the force magnitude it needs to fly to the next point in the flight path. Once lift and angle of attack (AOA) is calculated and the aircraft orientation is defined with the acceleration from the previous point. Allowing the rest of the load variables to be calculated such as the aircraft drag load (C_D^k), tether drag ($C_{D,eff}^t$), gravity (g) and previous acceleration from the last point. The force due to gravity is from the mass of the aircraft M_{air} summed with the mass of the tether based on the length (\bar{l}) and diameter (d) of the tether time. The previous acceleration is based on the acceleration vector seen at the previous point. The configuration is then all recalculated and tangential velocity is determined for the distance between points. That distance combined with the velocity provides the time interval between points. Also, as stated earlier, there is no acceleration in the radial direction the new tension on the tether is calculated for that point of flight.

The energy (E_i) per discrete point is then calculated by multiplying the tether tension times the predefined reel-out speed (RS). The power generated (P_i) is evaluated by dividing the work energy by the elapsed time dt from point to point using the following relationships.

$$E_i = T_i RS \quad P_i = E_i/dt$$

The total power generated is the summation off all of the individual segments. The total summation is part of a iterative loop which continuously calculates the loads at different section of the flight path until the max height constraint is met. Then the total energy is summed to determine the energy generated and the energy cycle ends.

With the energy cycle completed the reel-in cycle begins which consumes a fraction of the power generated. Power is consumed during the reel-in process which the kite is brought in through a straight trajectory. The kite is reduced to the minimum lift required to stay airborne reducing the energy required for retraction. Using the orientation and aerodynamic coefficients the tension of the tether is calculated using the following equation:

$$F_T = \sqrt{D^2 + L^2}$$

This function represents is the force vector of the aircraft in its lowest drag and lift configuration. The time required to draw the kite in is the total cable length divided by a reel in speed which is pre-defined. The work (W) done to bring the kite is the tension (F_T) of the aircraft times the cable length (CL_{RI}) and then the total power (P_{RI}) is the work divided by the total time (t). As shown in the series of equations below.

$$W = F_T * CL_{RI} \quad \text{and} \quad t = \frac{CL_{RI}}{RI_s}$$

$$P_{RI} = \frac{W}{t}$$

The total power generated for the cycle then is the sum the power generated, and the power used by the retraction phase. ⁶

The VLM data was used for the two geometries with the same wing area, aircraft mass and flight path. The ASK 21 glider was able to generate higher tether tensions and fly more iterations. The higher tether tensions are due to the higher speeds reached by the ASK21, generating larger tether tensions. When compared with the delta wing, which has a considerably lower coefficient of lift, the aircraft only succeeds in going through four cycles. The reduced cycles are attributed to the higher drag and lower lift the aircraft generatres, causing the aircraft to fly at lower velocities. The lower velocites results in the aircarft flying less figure eight patterns.

Demonstrated by the earlier equation where $F_{T,max}$ is a function of the apparent velocity squared and the aerodynamic coefficients.

As shown in Table 3.1 the net power produciton for the Delta wing at 20 m/s was 30.6 kW while the ASK 21 Glider generated 637 kW under the same conditions. Higher wind velocities showed an substancial increase in power generation. The Delta wing was not capable of generating enough lift with a 5 m/s wind to fly the prescirbed flight path.

Table 3.1: The power generation of the Delta Wing and ASK21 Glider with 5, 10, 15, and 20 m/s winds. The results are compared to Loyd's lift model.

Wind Speed [m/s]	Delta Wing [kW]		ASK 21 Glider [kW]	
	Simulation	Loyd's lift model	Simulation	Loyd's lift model
5	NA	1.53	14.7	29.2
10	2.29	12.2	102	233
15	12.9	41.3	301	788
20	30.6	97.9	637	1870

When compared to Myles Loyd's power generation equation for cross wind lift mode model, which is considered 100 % efficient. Comparing delta wing at wind speeds of 15 and 20 m/s we

see 69 % loss of of the power from Loyd's simplified model. The ASK21 geometry was similar, with a percent power loss of 62 %, and 66 % of Loyd's simplified lift model. These results are similar to what was discovered by Myles Loyd's model and other models which have showed losses of 66 % from tether drag. Consequently, showing the details of the more complicated model are reasonable. When comparing the two geometries at different speeds, observations show the power generation begins to converge. At 10 m/s wind speeds the delta wing generates 2.2% of the power of the ASK 21 geometry. As wind speed increases to 20 m/s the total power percentage increases to 4.8 %. At lower wind speeds, geometry of the aircraft has a larger effect on the power generation. Overall the ASK 21 glider generates considerably more energy.

The model is optimistic in its estimation of the power generation leaving room for further improvement. It is optimistic primarily due to: 1) the model assumes a hundred percent efficiency when considering the conversion of kinetic energy to electrical energy, 2) dynamic effects are not considered, including increased drag due to the aircraft yawing, 3) the tether model assumes a rigid element which reduces drag while the tether in reality sags, and 4) sideslip isn't taken into consideration which can significantly increase the drag depending on the geometric shape of the aircraft. The simulation can improve further but shows a strong agreement with previous static power generation models in regard to the 70% power loss due to tether drag and weight. The results of one of these studies is shown in the orange when considering the $F_{T,max}$ and using that to calculate the tether tension seen by the aircraft.

3.1.3 Performance Characteristics

Additional flight characteristics need to be estimated due to the assumption of the power generation code that the aircraft can fly the prescribed flight path. Using flight performance

characteristics, the flight path can be determined if it is viable. The primary flight characteristics evaluated is pitch stability. Pitch or longitudinal stability begins with an investigation into the moments in the y-axis through the center of gravity and their variation with airplanes coefficient of lift. In order to have equilibrium these need to sum to zero which is critical when looking at controlled flight. A pitch stability model is derived and used to evaluate the effects of the bridle, tail size, and geometry on pitch stability of the aircraft.

Stability problems such as equilibrium, static stability, and control are often very complex and can be simplified to very important static equations of moments about the axis of the aircraft through the center of gravity. These equations are critical for the initial development to design an aircraft for adequate stability and control characteristics. Stability theory was first developed and simplified using the case of fixed controls (stick-fixed) and an aircraft in gliding flight. Theory of stability requires an investigation into the moments about the airplane's axis, for pitch stability the moments are evaluated about the Y axis while directional stability considers moments about the Z axis of the aircraft. The use of a tether in AWES applications adds another variable which has not been considered before. This research derives a new pitch stability equation which accounts for the bridle and provides the advantages of using such a system. Throughout this section any aerodynamic elements are assumed to be represented with a mean aerodynamic chord, loads, and moments acting at their aerodynamic center. The loads are further simplified into the lift and drag of the element acting at the aerodynamic center, with a pitching moment about the aerodynamic center. Typically, the aerodynamic center of an airfoil is close to quarter chord of the airfoil. For this reason, the center of gravity of the aircraft is usually located close to quarter chord of the main element.

Pitch stability is the aircraft's tendency to maintain an angle of attack and airspeed and is evaluated by the summation of the moments about the Y axis. For an airplane these contributions come from the main element, fuselage, and horizontal stabilizer. For a standard aircraft the center of gravity and the horizontal tail size and position being the dominate factors affecting the stability. With a center of gravity farther forward an increase in stability but more resistance to angle of attack and velocity changes. While the horizontal stabilizer is sized using the horizontal tail volume coefficient (V_h) which for most well-behaved aircrafts typically ranges from 0.3 to 0.6 and can be calculated using the equation:

$$V_h = \frac{S_h l_h}{S c}$$

Using the horizontal stabilizer area (S_h) and the moment arm length (l_h) divided by the wing area (S) and the average chord length (c). The horizontal tail sizing affects the neutral point location; if the horizontal tail volume coefficient is too small, the pitch behavior will be very sensitive to the center of gravity location. The neutral point is where the center of gravity location which neutral stability is achieved defined later. The horizontal stabilizer is similar to how the vertical tail provides yaw dampening and the dihedral angle provides spiral stability.

The stability equation begins with the summation of loads resulting in the moments on the aircraft. To resolve the loads on the aircraft they are put into the airplane reference frame. For wing elements the loads are transformed into the reference frame using the following equations:

$$N = L \cos(\alpha - i) + D \sin(\alpha - i)$$

$$C = D \cos(\alpha - i) + L \sin(\alpha - i)$$

The following put the equations into the normal and chord wise loads of the elements. With L being the load due to lift and D being the load from drag. The angle of attack (α) is then

subtracted by the angle of incidence of the wing (i) which is with respect to the aircrafts reference line. Then, the summation of the moments about the center of gravity of the aircraft is obtained:

$$M_{cg} = M_{main} + M_{fus} - M_{tail} + M_{te}$$

The contribution for the moment about the main element is:

$$M_{main} = N x_{aw} + C z_{aw} + M_{ac}$$

Allows the normal and chordwise moments to be calculated as well as the pitching moment (M_{ac}) of the airfoil. The same equations are used for the horizontal stabilizer however as shown below while using the length of the tail (l_t).

$$M_{tail} = N_t l_t + C_t h_t + M_{ac t}$$

However, the pitching moment and chordwise moment caused by the tail are found to be negatable compared to other loads, thus they are not used. The moments induced by the fuselage are:

$$M_{fus} = N_{fus} x_{af} + M_{fus}$$

The effects are primarily ignored in the program as the fuselage should have negligible effects because they are just used to connect the main element the tail elements. However, with more information and refined design, they are an optional input. In addition to this equation is the moments induced from the bridal system are calculated using the following equation.

$$M_{te} = T_1 d_1 \sin(\theta_1) + T_2 d_2 \sin(\theta_2)$$

The load paths for the tether are shown in Figure 3.7 show how the tension (T) of each line are configured to the aircraft. To calculate the moment the distance to the center of gravity is used as well as the angle the tether makes to the center line of the aircraft.

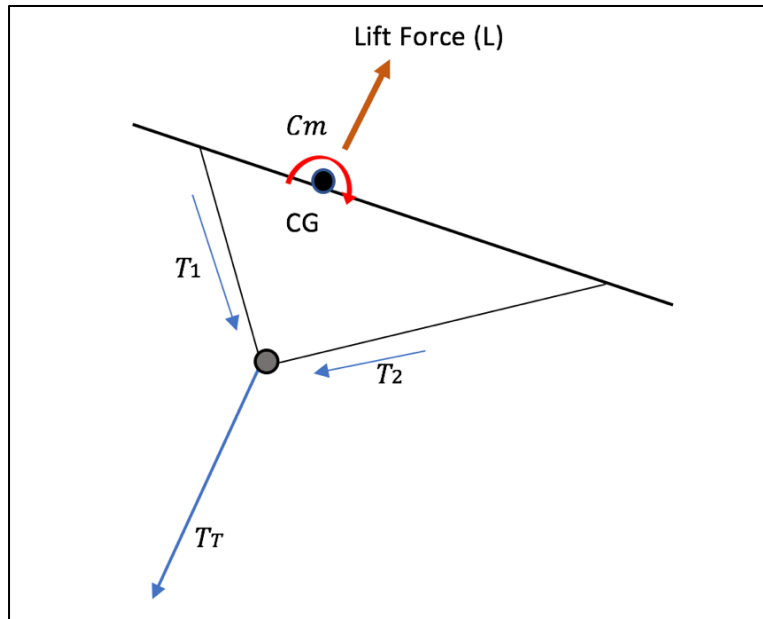


Figure 3.5: Loading conditions due to aerodynamic

For equilibrium to be achieved the moment about the center of gravity (M_{cg}) have to be equal to zero. It is necessary to place this equation in coefficient form by dividing through with dynamic pressure (q), the wing area (S_w) and the mean aerodynamic chord. To take into effect loss of energy from interactions of the wing and fuselage the tail efficiency factor (η_t) is used which is the ratio of tails dynamic pressure (q_t) to the main elements dynamic pressure (q). After the equation is put in to coefficient from the pitching moment coefficient (C_m), plotted against the coefficient of lift, is used to calculate the static pitch stability of the aircraft. For an aircraft to be to stable the slope of the pitching moment coefficient (C_m) versus coefficient of lift must be negative.

Once the equation for the pitching moment coefficient is derived the derivative is taken with respect to the coefficient of lift which provides the slope of the pitching moment curve ($\frac{dC_m}{dC_L}$).

Shown in the equation below the pitch stability of the aircraft is shown based on the four different contributions of the wing, fuselage, horizontal stabilizer, and bridle.

$$\frac{dC_m}{dC_L} = \underbrace{\frac{dC_N}{dC_L} \frac{x_a}{c} + \frac{dC_c}{dC_L} \frac{z_a}{c} + \frac{C_{mac}}{dC_L}}_{\text{Wing}} + \underbrace{\left(\frac{dC_m}{dC_L}\right)_{\frac{Fus}{Nac}}}_{\text{Fusilage}} - \underbrace{\frac{dC_{Nt}}{dC_L} \frac{S_t}{S_w} \frac{l_t}{c} \eta_t}_{\text{Horizontal Stabilizer}} + \underbrace{\frac{dC_{T1}}{dC_L} \frac{d_1}{c} \sin(\theta_1) + \frac{dC_{T2}}{dC_L} \frac{d_1}{c} \sin(\theta_2)}_{\text{Bridle}}$$

As stated earlier, the slope of the pitching moment curve $\left(\frac{dC_m}{dC_L}\right)$ must be negative to have static longitudinal stability of the aircraft. A negative slope creates a nose down pitching moment tending to reduce lift back to equilibrium. If the slope is positive the aircraft would have static instability and produce nose up moments tending to increase the coefficient of lift further, resulting in higher nose up moments. When the pitching moment slope is zero the aircraft is considered neutrally stable which occurs when the neutral point and center of gravity are at the same point. Pitch stability determines the ability to maintain an angle of attack and speed. With increased stability, the aircraft is more resistant to angle of attack and velocity changes while decreased stability means less resistances. Thus, for a highly stable aircraft larger elevator trim or airspeed change is going to be required to change angle of attack when compared to a weakly stable aircraft, which will be more difficult to control.

The code compares the effects of a bridled aircraft to a free flying aircraft while evaluating the effects of the tail. The assumptions used are: 1) bridled tethers cannot support compressive load, 2) bridled angles does not change, 3) the load along the chord and moment around the center of pressure of the tail are negligible, and 4) the tether and bridled do not yield. The two equations apply to two AWES designs: 1) The AWES use a bridle for stability and control and 2) the AWES use a horizontal stabilizer with a tether mounted to its center of gravity. As shown below the Delta wing exhibits a positive pitching moment of $.013 \frac{dC_m}{dC_L}$ without a tail, meaning it is

unstable. The ASK21 geometry was less stable with a pitching moment of $.025 \frac{dC_m}{dC_L}$ using only the main element. With the increase in tail size and length the pitch stability both geometries became increasingly stable. With the addition of the bridal system with the geometry having the front tether .24 meters from the CG and an angle of 60 degrees. The aft tether had a length .5 meters from the CG and an angle of 20 degrees.

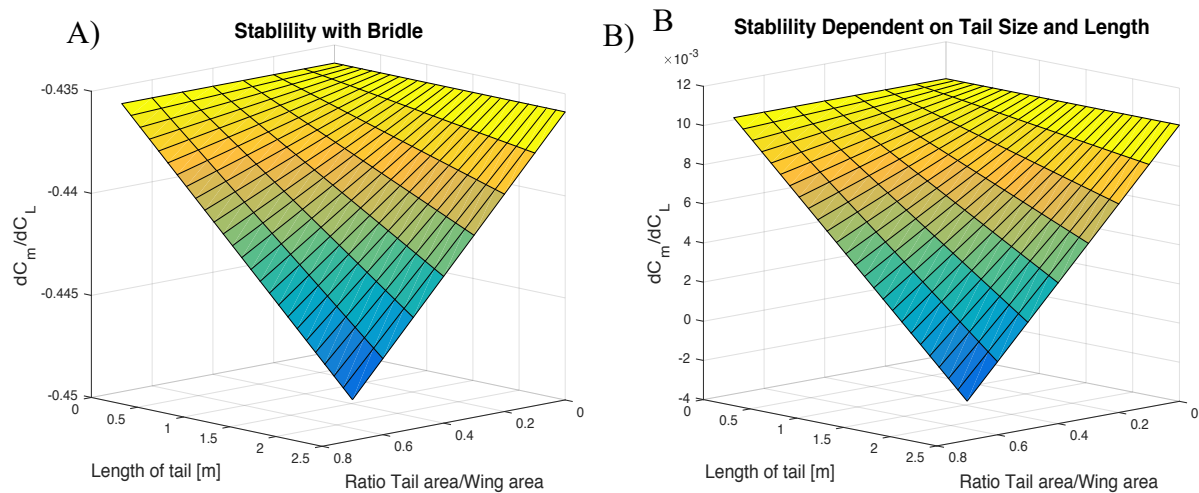


Figure 3.6: Stability of the Delta wing geometry A) pitch stability with bridal, tail length and area ratio. B) without the effects of the bridal.

The stability of the Delta wing geometry increased from 0.010 to $-0.435 \frac{dC_m}{dC_L}$. The addition of the same bridal system resulted in an increased stability from $.025$ to $-0.0425 \frac{dC_m}{dC_L}$ for the ASK 21 geometry.

Using the ASK21 geometry, the bridal geometry was analyzed. The two geometric constraints explored are the distance from the CG and the angle to the chord of the aircraft. The distance from the center of gravity has a linear effect on the stability. As the distance increases from 0 to 0.5 meters from the CG for the front tether the stability increases substantially. However, as the distance increases from 0 to 0.5 meters for the aft tether the stability decreases substantially. With the angles set to a constant 20 degrees. The distance from the CG shows a linear trend but

acts as a scalar for the effects of the tether angles. The angles of the bridal also significantly affect stability.

The bridal angle shows a similar trend to the CG offset of the tethers. As the angle increases, for the front tether, from 0 to 90 degrees the stability increases but as the angle approaches 90 one sees diminishing returns. The aft angle has the inverse affect with increasing gains as the angle decreases from 90. The plot shown used offset distances of 0.01 meters from the CG. With the high-tension loads seen on the tether combined with the bridal's offsets from the CG the bridal moments can easily dominate the moments acting on the aircraft. The dominate loads allows the bridal to determine the pitch stability of the aircraft and have an increasing affect with larger CG offsets, resulting in the ability to tune the pitch stability of the aircraft with the bridal, as shown in Figure 3.9. The center of offset of the two bridals was set to 0.01 meters.

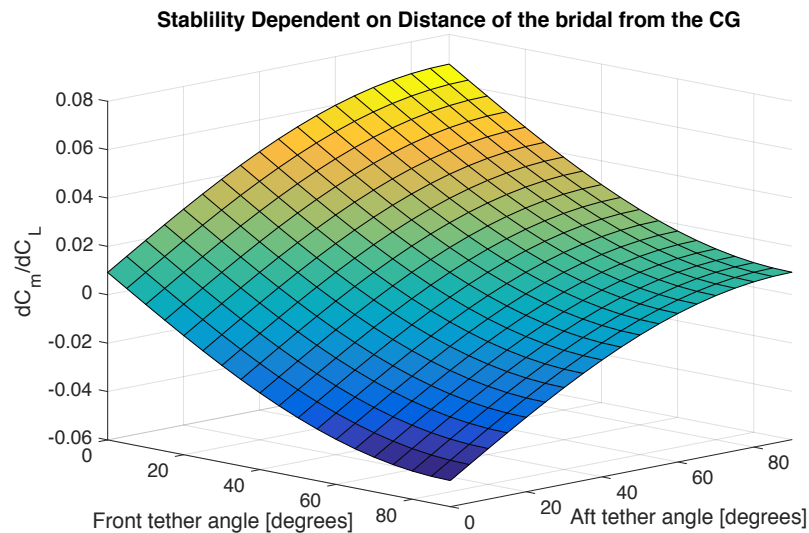


Figure 3.7: Stability of an aircraft based on bridal geometry dependent on the bridal angle using a CG offset of 0.01 meter.

A strong example of the ability to set a specific pitch stability using the bridal system is shown by the adjusting the bridal geometry to have neutral stability. Using the derived formula, the

bridal configuration for the ASK21 geometry without a tail would be: the front bridal would be mounted 0.05 m from the CG with a 29-degree angle and the aft bridal 0.1 m with a 12-degree angle. For the delta wing geometry without a tail the front bridal would be mounted 0.05 m with an angle of 18 degrees and the aft bridal mounted at 0.1 m with an angle of 8 degrees.

3.2 Wind Tunnel Study

This section will discuss the wind tunnel study conducted at Oregon State University using the closed loop wind tunnel. The test article used is the delta wing geometry used in the VLM simulation discussed earlier. Although the geometry produces lower coefficient of lift it has a high degree of maneuverability with minimal side slip due to its large dihedral angle. This study runs a static angle of attack sweep from 0 to 90 degrees to experimentally acquire the aerodynamic coefficients through the linear region and at high angles. The coefficient of lift and drag are evaluated. The linear region is compared to the VLM data and the aerodynamic coefficients of the delta wing at high angles of attack are evaluated.

3.2.1 Experimental Setup

The experimental setup is comprised of the wind tunnel, data acquisition, and the test article. Oregon State University's low speed, and closed loop wind tunnel uses a closed test section measuring 1.3m high, 1.6m wide and 10 m long. A variable pitch propeller, controlled by a variable frequency converter, providing flow velocities between 4 m/s and 20 m/s. Experimental characterization of the wind tunnel's test section showed average turbulence intensities below 1%. The low intensities are achieved by having the flow pass through a series of honeycomb screens and then accelerated through a converging region before entering the test section.

Data acquisition, tunnel operation, and angle of attack settings are managed using a LabVIEW program. The LabVIEW program processes forces, moments, dynamic and static pressures, air temperature, and arm position. Forces in the x, y and z body frame directions, as well as the moments about the x, y and z axes, were measured using a six axis JR3 load cell. Airspeed was recorded using a pitot tube and pressure transducer. Temperature was measured using an RTD temperature probe. An optical motor encoder was used to record the servo motor position for angle of attack. The sensors listed above were all sampled at 500 Hz.

The model is a 1:1.75 scale model of the delta wing kite, manufactured using acrylic panels and epoxy. The wing elements are rigid using a flat panel airfoil with an aerodynamic chord of 12.7 cm, wingspan of .57 m, and an airfoil thickness of 6.35 mm. The model was held near the center of the freestream using a u-shaped aluminum arm, shown in Figure 3.10. The support arm is attached to a servo motor which allows precise control of angle of attack using the optical motor encoder and LabVIEW program. For high angles of attack an angle offset is used at the joint of the support arm. Using an inclinometer, the angle was measured at the root of the JR3 to have accurate angle control.



Figure 3.8: The Oregon State University closed loop wind tunnel with stunt kite test geometry.

3.2.2 Results

High angle of attack conditions, typically at take-off and landing, were replicated through an angle of attack sweeps between -2° and 90° at three Re numbers. The Aerodynamic coefficients are illustrated in Figures 3.11 and 3.12. Results show that, at very high angles of attack, which typical aircraft don't fly at, the C_L is higher than regular airfoils, despite the wing being comprised of flat plates. Typical airfoils used for wind turbine blades exhibit a shallow delayed stall⁸⁷. The main cause can be attributed to the delta shape of the low aspect ratio wing. Using the unique anhedral and dihedral section of the wing the aircraft generates strong wing tip vortexes which decreases flow separation at high angles of attack. Where typical aircraft begins to generate positive lift at an AOA of 0° the delta wing geometry doesn't begin to generate positive lift until an AOA of 10° and also has a delayed stall compared to the other airfoils. Generating lift at such a high AOA give the aircraft the unique ability to have a vertical take-off. The high lift results in high tension values during take-off providing early control and stability of the aircraft.

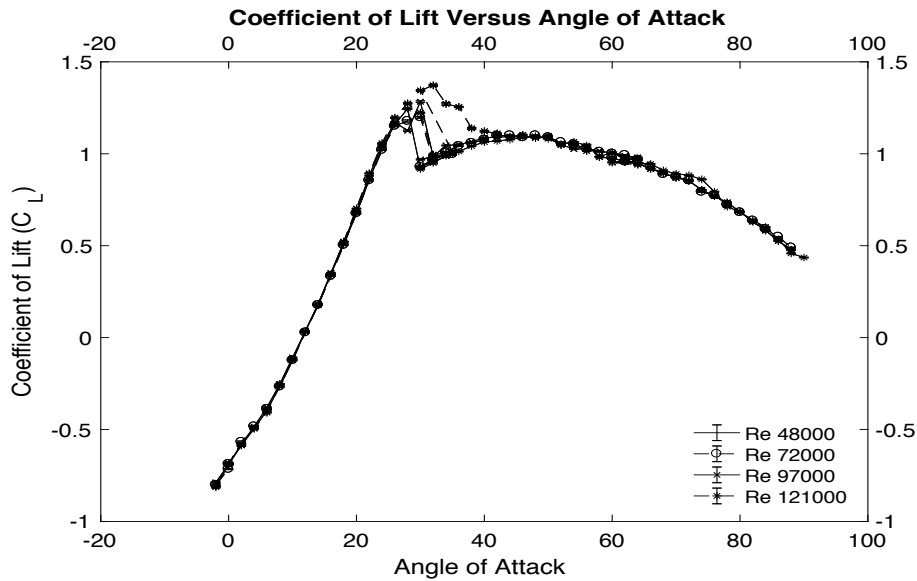


Figure 3.9: Angle of attack sweep vs coefficient lift.

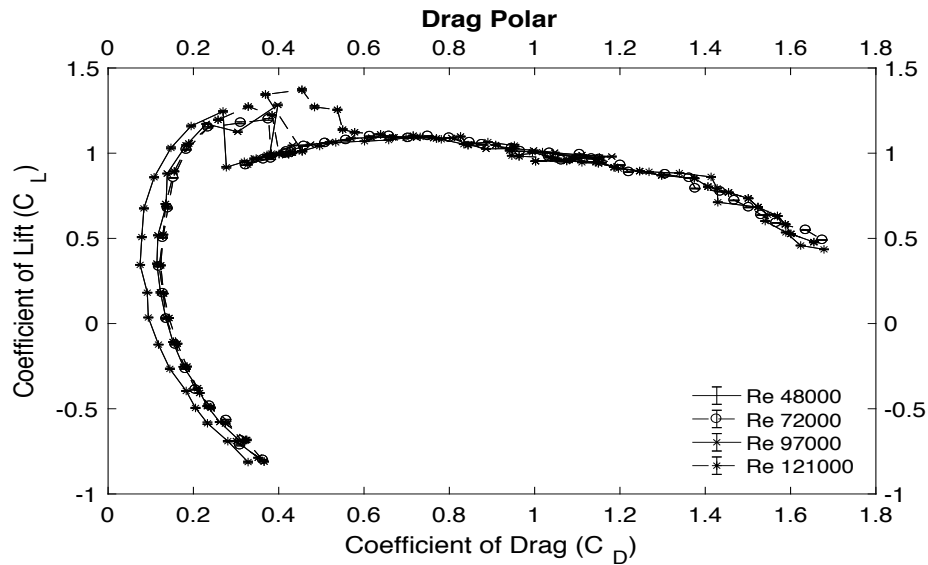


Figure 3.10: Drag polar of delta wing configuration.

4. Thermal and Mechanical Testing of Carbon Fiber Reinforcement

Prototyping is critical for the development of AWES as it's difficult to model dynamic fluid interactions. Shown by some of the most successful startup companies Ampyx Power and Makani have developed a minimum of seven different wing prototypes. Ampyx developed three different full-scale prototypes and are verifying a fourth in 2019. While Makani doesn't state much about their prototype development, they tested a series of smaller prototypes which preceded their larger scale 600 kW test turbine. Such designs consist of complex geometries and need to withstand loads that can occur from the environment. To minimize the energy loss due to gravity, the weight of the AWES needs to be minimized. Many materials often used for prototyping are either too heavy, do not meet the structural requirements, or are too time consuming to fabricate prototypes. Especially since the optimal design would have a large aspect ratio, meaning a small mean chord length and long span. Those physical constraints make structural design difficult. For this reason, due to the high specific strength and stiffness of high-

performance fibers, composites were chosen. The materials used also exhibit strong structural, thermal, and environmental resistances.

Certified by the Federal Aviation Administration (FAA) high modulus fibers have been used extensively in the aerospace and wind turbine industry. Prepreg shows significant advantages due to its high fiber to resin ratio, significantly improving the specific strength and stiffness of the composite laminate. When using sandwich panels, the flexural stiffness and strength also significantly increases with minimal weight increase. The largest difficulty with implementing composites is manufacturing and initial investment. Tooling costs and performance increase significantly as part performance increases which makes complex geometries and one-off prototypes impossible without significant investment. To rapidly prototype AWES a new hybrid manufacturing technique is developed using composites.

This research focuses on the development of this new hybrid manufacturing technique which uses a 3D printed structure as the mold and core structure for the composite sandwich panel. Allowing complex geometries to be designed and manufactured, while reducing the time and cost restraints for conventional manufacturing techniques. This method allows the load paths, core structure, and bonding surface to be independently designed especially when paired with techniques such as topology optimization. As shown in the literature review, a variety of studies have looked into reinforced 3D printed structures, using long fibers. Findings showed that reinforcement improved stiffness and strength; however, the part show low interfacial bonding between the fibers and the 3D printed polymer. The interfacial bonding strength has tried to be improved with the addition of sizing agents, but the specific flexural strength and flexural stiffness are still lower than that of composite sandwich panels.^{75,74} For this technique to be viable, the 3D printed material must be able to withstand the high temperatures, that can occur

during the cure process from the oven and exothermic reaction during crosslinking. Additionally, the polymer must have strong adhesion between the composite face sheets and the printed core structure. These characteristics are critical to maintaining high tolerance parts, while having a high specific strength and stiffness of the sandwich structure. For this reason, a series of thermal and mechanical tests were conducted to determine the viability of this manufacturing technique.

The materials used for the development of this rapid prototyping technique have been consistently used in industry but never combined to form a composite material. The materials used consist of carbon fiber, epoxy resin system, epoxy film adhesive, and Nylon (PA12) printed core structure. The T700S fibers are Toray’s high modulus fiber used for specific aerospace application and are FAA certified. Commonly used by companies such as Boeing, the fibers have been extensively tested and previously used by Nanya Li et al. in the reinforcement of 3D printed materials ⁷⁴. The T700S fiber are prepregged with Toray’s 2510 epoxy resin system which is developed for primary structures in aerospace applications. The out of autoclave cure resin system has excellent structural and thermal properties allowing it to be used in elevated temperatures. With a lower temp cure ranging from 121 to 132 degrees centigrade, Figure 4.1.

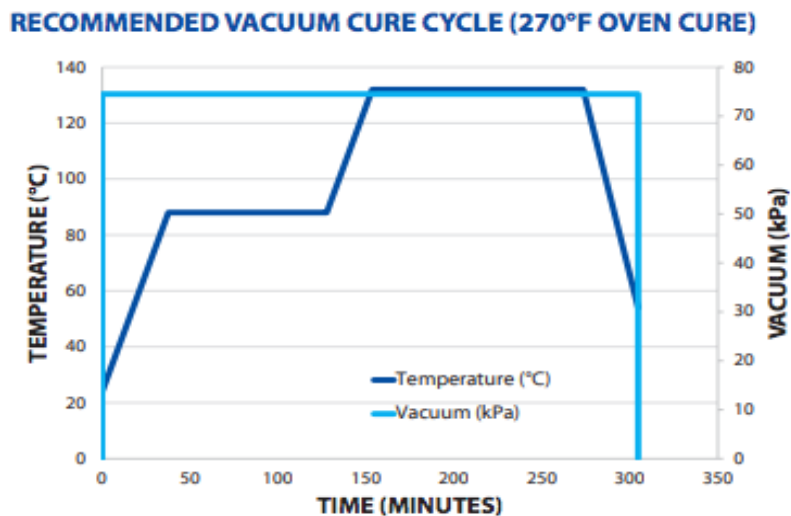


Figure 4.1: Toray 2510 semi toughened out of autoclave (OOA) epoxy cure cycle which offers a curing range from 250 to 270 degrees F or 121 to 132 degrees Celsius ⁸⁸

The lower temperature and flexible cure cycle make the resin ideal for processing with the 3D printed core as elevated temperature are a concern due to the exothermic reaction of the epoxy. Henkel 9696.06 film adhesive is used to bond the laminate face sheets to the core. Designed originally for bonding to honeycomb core structures, the film adhesive excels with a high strength, stiffness, and fatigue life. With an emphasis on toughness and environmental resistances and compatibility with cure temperatures of the 2510 resin system, the adhesive possesses ideal qualities for this manufacturing application. Strong adhesion between the face sheets and core structure is the most important variable to ensure optimal performance of the sandwich panel. The core structure is made out of polyamide 12 (PA12). Polyamide was chosen due to its wide use, strength, toughness, stiffness, abrasion resistance, and retention of physical and mechanical properties over large temperature ranges. Developed by HP, the manufacturing process is similar to printer-based 3D printing which they call Jet Fusion. Printing a fusion agent onto the powder bed causes the material to conduct heat better. A lamp is used to heat and sinter the specified sections. The method relies on very accurate heat control through the material when using the fusing agent. The PA12 has higher thermal resistance than what is typically seen with most 3D printed materials making it an appropriate material choice for this project. Also, when using HP's multi jet fusion process print time is minimized, higher tolerance, and higher density are achieved then with other 3D printers. Typical coordinates were used for the 3D printer with the X oriented along the front of the printer, Y oriented into the depth of the printer, and the Z direction oriented vertically.

Polymers are classified into amorphous and semi crystalline, PA12 is a semi crystalline meaning a percent of chain molecules are arranged in an orderly structure with the remainder in a disordered amorphous state. The percent crystallinity is also controlled with processing

techniques during the heating and cooling cycle. Semi crystalline and amorphous polymers have significantly different thermal and mechanical properties due to their aggregation structure. The lack of a crystal structure results in amorphous materials only exhibiting a glass transition temperature while semi crystalline polymers exhibit crystallization temperatures and melting temperatures. Increased percent crystallinity has also shown to increase the stiffness and mechanical strength of the polymer.

4.1 Thermal Characterization of PA12

The 3D printed PA12 is characterized using two thermal characterization techniques, thermogravimetric analysis (TGA) and differential scanning calorimetry (DSC). TGA is primarily used to determine the composition of the polymer in question and can help determine additives and volatiles within the material. DSC can be used to determine critical temperatures and micro structures of the PA12. Especially important is the melting temperature and the percent crystallinity of the PA12. These two characteristics determine if significant deformations will occur and micro structure of the PA12.

4.1.1 Thermogravimetric Analysis (TGA)

Thermogravimetric Analysis (TGA) is useful in performing compositional analysis which the amount of highly volatile matter, medium volatile matter, combustible material, and ash content of compounds are measured. Using a controlled inert and reactive gas environment the weight percent of individual components can be determined. The mass of the sample is recorded as a function of temperature while heated in a controlled environment. The mass loss through specific temperature ranges provides the compositional data of the sample. This technique is commonly used in industry for material screening and quality control applications such as: 1) carbon to polymer ratio ranges are required in some elastomeric and plastic parts to adjust mechanical

properties and 2) the addition of inert compound such as filler, ash, or other reinforcement to tailor polymeric material. The equation used to determine the percent mass loss depends on original mass of the specimen (W), mass measured at a specific temperature (R) and, highly volatile matter content (V) as a received basis percent.

$$V = \frac{W - R}{W} * 100$$

Medium volatile matter content (O) is dependent on mass measured at the initial temperature (R), mass measured at the next sequential temperature (S) and the original specimen mass (W).

$$O = \frac{R - S}{W} * 100$$

This process is continued for combustible material content until the total composition of the material is determined.

The TGA is used to determine the composition of the 3D printed PA12. HP's jet fusion printing process adds binder to the PA12, in addition to the nylon which can absorb water. The presence of water can significantly affect the bond strength as well as other impurities can affect the mechanical properties. Using TGA helps determine if additional drying process needs to be applied, before bonding the sandwich structure. Another concern is the addition of the fusion agent as it affects the mechanical and thermal properties of the PA12. Also, large amounts of can volatile during the curing process severely lower the bond quality. Understanding the final parts composition helps predict difficulties that can occur during the curing process.

4.1.1.1 *Experimental Setup*

ASTM standard E 1131 was followed to evaluate the compositional analysis of the PA12 samples. Five samples were generated from 3D printed parts which were stored at room

temperature and exposed to the atmospheric environment, similar to an assembly line for three months. No additional processing had been done to the samples aside from the printing process. A razor blade was used to shave off filaments of PA12 from different sections. HP's fusing agent uses carbon platelets due to its ability to conduct thermal energy and allowing it to sinter the material giving the material the black color. To avoid heterogeneity within the material the shavings of the material are taken from randomized locations from the large parts. Five samples are generated consisting of 15 *mg* of PA12 derived from the shavings. Before adding the samples to the crucible for testing the TGA is zeroed and tarred with the crucible.

TA instruments TGA Q500 was used for the analysis of the PA12 with a weight precision of $\pm 0.01\%$, sensitivity of 0.1 μg , and temperature range from ambient temperature to 1000 °C making sure the PA12 can be fully decomposed. The environment is further controlled by having a constant flow of nitrogen to purge the system of oxygen. At high temperatures the presence of oxygen can result in a combustion reaction causing the volatile content to be inflated. The deoxygenated environment prevents the high percent weight loss, providing accurate results. TGA temperature sweep is from room temperature up to 600 °C at a rate of 10 °C/*min*.

TGA data is postprocessed using TA Universal Analysis Software. The software plots the percent weight loss versus temperature. The percent weight loss is determined for each temperature segment as discussed earlier providing information on the water, carbon and polymer content. The confidence interval is determined by using a t-distribution which is used when the sample size is less than 30. This incorporates the fact a smaller sample size gives a larger distribution. Assuming the data is normally distributed the following equation can be used to evaluate the confidence interval:

$$\text{Confidence Interval} = \bar{X} \pm t \frac{s}{\sqrt{n}}$$

The equation is dependent on the mean value (\bar{X}), t-distribution value (t), the standard deviation (s), and the sample size (n). The t-distribution is dependent on the degrees of freedom (df) of the sample which is 9 in the case of this study and is envaulted using the sample size.

$$df = n - 1$$

The t-distribution is used throughout all the mechanical and thermal tests to evaluate the confidence intervals.

4.1.1.2 Results

The TGA results show four distinct areas shown in Figure 4.2. The initial weight drops with increased temperature especially after 100°C to 325°C, a high volatile drop from 325°C to 400°C, medium volatile matter from 400°C to 500°C, and a low volatile content from 500°C to 600°C. These segments can easily be segregated into some of the basic components of the PA12. The initial weight percent drop after 100°C is the water content absorbed by the PA12, which is followed by another highly volatile material most likely a bonding agent used during the printing process. The next mass drop is representative of the PA12 which shows the largest weight composition at 80%. The last segment are the carbon platelets used in the bonding agent.

Sample: PA12_3
 Size: 12.9300 mg
 Method: CIRELAB_SMOLDER

TGA

File: F:\AlbLab_PA12_TGA\PA12_3
 Operator: Alex Train
 Run Date: 09-Oct-2018 17:27
 Instrument: 2950 TGA HR V6.0E

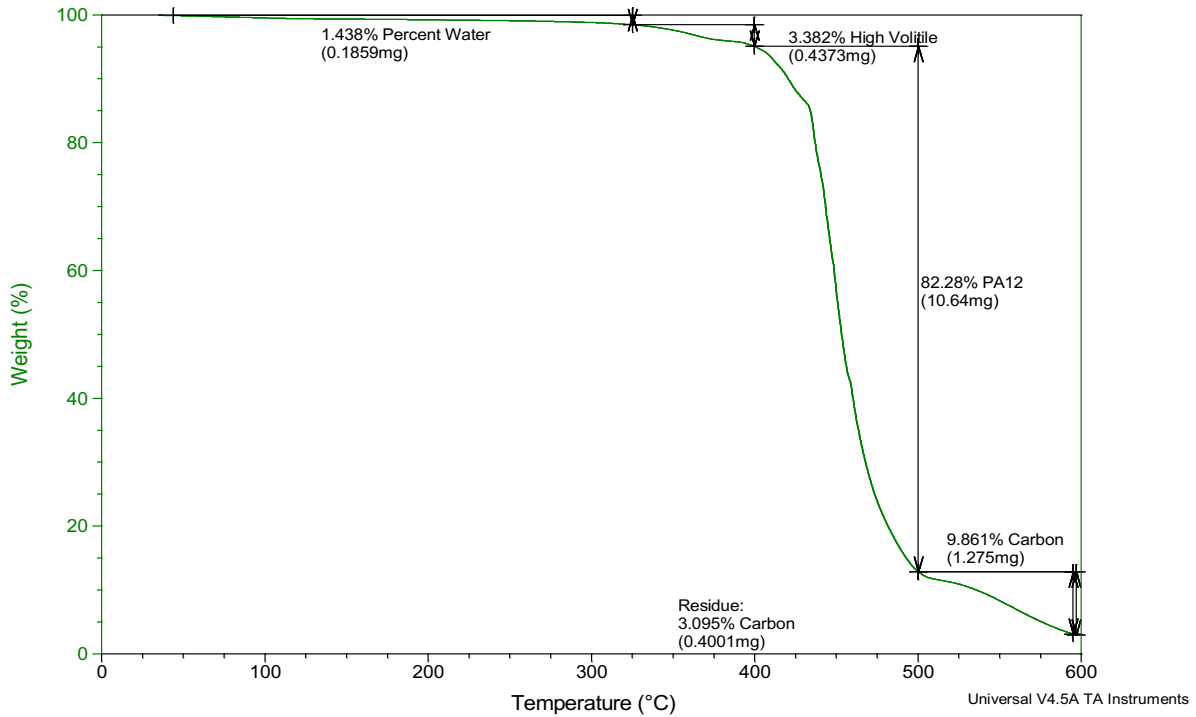


Figure 4.2: plot of thermogravimetry to determine the weight percent composition of PA12, carbon black, and other. The composition breaks down of the 3D printed PA12 is shown in Table 4.1.

Table 4.1: The composition of the PA12 3D printed parts determined using the TGA.

Material	The Weight Percent [%]	Temperature Region
Water	1.5 ± 0.12	100°C – 325°C
Bonding Agent	4.1 ± 2.2	325°C – 400°C
Nylon PA12	80. ±4.0	400°C – 500°C
Carbon	8.8 ± 1.4	500°C – 600°C
Carbon Residue	5.3 ± 3.3	600°C +

Through this process, we can see that the material is primarily PA12 with a filler fraction of 20.8%. With the sample absorbing 1.5 % water from the atmosphere.

4.1.2 Digital Scanning Calorimetry (DSC)

DSC is a common polymer thermal characterization technique. The DSC measures the endo and exothermic reactions as a polymer changes phase. Using this technique, a heating and cooling

curve is generated providing the glass transition temperature (T_g), initial melting temperature (T_i), curing temperatures, crystallization temperature (T_c), percent crystallinity, and enthalpies (ΔH) associated with these processes. Depending on the polymer manufacturing process internal stresses can be introduced through large temperature gradients or quench cooling the material. The residual stresses are exhibited by noise being introduced at the glass transition temperature. The main concern is that the melting temperature of the PA12 is not exceeded during the curing process. Therefore, an accurate measurement of the initial melting temperature is especially important to this manufacturing technique. Additionally, a high percent crystallinity and low residual stresses makes sure that the material is going to perform optimally. The percent crystallinity is measured by running a heating cycle followed by a quench cooling. Then, the following equation is used to measure the percent crystallinity.

$$\% \text{ crystallinity} = \frac{(\Delta H_m + \Delta H_c)}{\Delta H_f (1 - f)} 100$$

Which ΔH_m the heat of fusion, ΔH_c is the cold crystallization, and ΔH_f is the heat of fusion for a fully crystalline material, which for PA12 is 245 J/g. Additionally, the crystallinity fraction (X_c) is determined using the following equation:

$$X_c = \frac{\Delta H_c}{\Delta H_c^o (1 - f)} 100$$

The crystallization enthalpy (ΔH_c) is divided by the full enthalpy of a crystallized sample (ΔH_c^o) while being scaled by the mass fraction of filler (f). The crystallinity fraction determines the potential for the material to be crystallized. Results from the TGA showed that the filler fraction was about 20.8%.

4.1.2.1 *Experimental Setup*

ASTM standard D3418 was followed for use in defining transition temperatures of polymers by differential scanning calorimetry. Samples were created in the same manner as TGA samples. Five samples were generated from 3D printed parts which were stored at room temperature in an environment that would be similar to an assembly line. To avoid addition of energy and changing of the structure a razor blade was used to shave off filaments of PA12. The shavings were taken from different areas of the specimens as to avoid heterogeneity within the printing process. Samples were 15 *mg* measured within 10 μ *g* and sealed within aluminum pans. The pans are hermetically sealed with an operating temperature from -180 to 600 °C. These samples were prepared for TA Instruments Q2000 series DSC.

The tests were conducted using TA instrument Q2000 series DSC which was outfitted with nitrogen cooling system, shown in Figure 4.3. The nitrogen cooling system allows the DSC to have a temperature range from -180 to 725 °C and has a calorimetric precession and reproducibility of 0.05%. The tests conducted had a heating cycle and quench cooling cycle for with the temperature was varied from 0 to 300 °C. The heating cycle used a heating rate of 10 °C/*min* while the cooling rate was 20 °C/*min*. These tests were conducted within an inert environment using nitrogen gas.



Figure 4.3: Differential Scanning Calorimetry Q 2000 series used to measure the exothermic and endothermic response of the polymer.

The DSC data was postprocessed using TA Universal Analysis Software. The software plots the exothermic and endothermic reactions with respect to temperatures allowing the thermal characteristics to be defined.

4.1.2.2 Results

The DSC heating cycle is, provides three areas of significance which determine the PA12's thermal characteristics and mechanical structure, see Figure 4.4, during the heating cycle the heat flow is negative with the T_g represented by a slight decrease similar to an S-shape. Initial melting temperature and enthalpy are represented by a large dip in the graph and the enthalpy is the integral of the process. The crystallization temperature and enthalpy occur during the cooling cycle and are represented by a large increase in heat flow as shown in one of the samples below.

Sample: ALBLab_PA12_DSC_C_CC_4-23
 Size: 11.0000 mg
 Method: shutdown

DSC

File: G:\ALBLab_PA12_DSC_C_CC_4-23.001
 Operator: Alexander Muschler
 Run Date: 23-Apr-2018 15:13
 Instrument: DSC Q2000 V24.10 Build 122

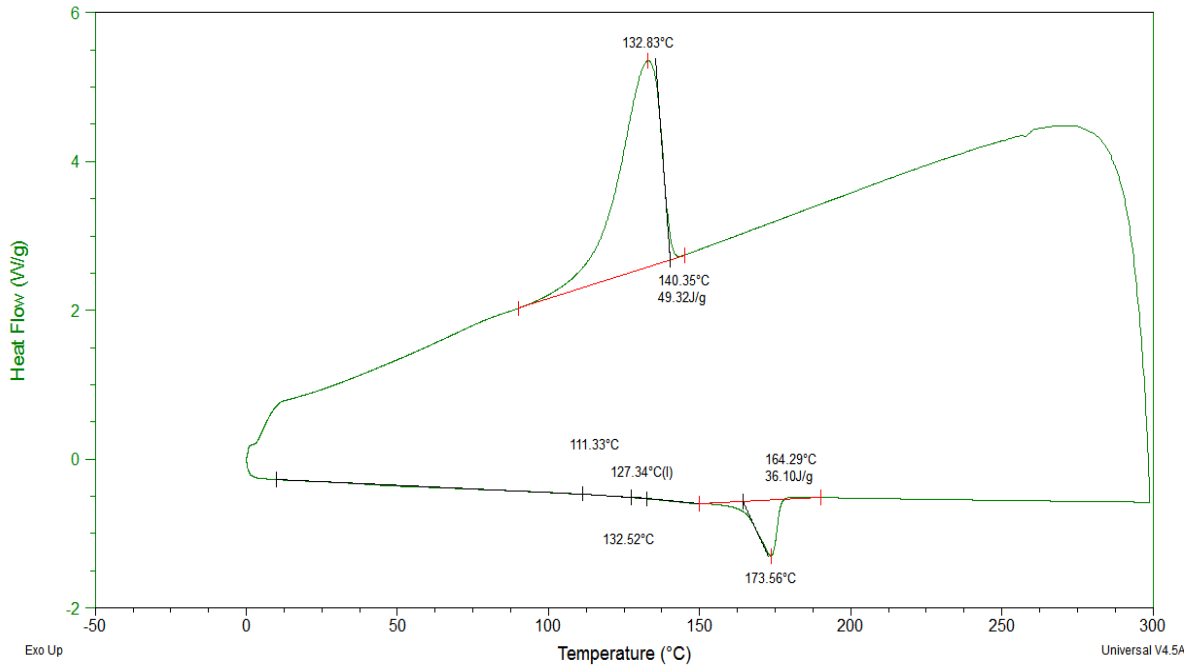


Figure 4.4: Differential scanning calorimetry slow cooled plot showing the glass transition temperature, the melting temperature and the crystallization temperature.

The Tg, initial melting temperature, enthalpies and crystallization temperature are represented in Table 4.2.

Table 4.2: Thermal characterization of the PA12 using the DSC.

Material	Tg [°C]	Melting Temperature [°C]	Crystallization Temperature [°C]	Melting Enthalpy [J/g]	Crystallization Enthalpy [J/g]
Nylon PA12	121.0 ± 3.7	177.9 ± 4.1	139.2 ± 8.2	52.0 ± 20	48.7 ± 2.4

The primary concern of using PA12 is the melting temperature, which cannot be exceeded during the cure cycle. The melting temperature is at 177.9 °C while the cure cycle for the T700 prepreg material does not exceed 132°C during the cure cycle. The melting temperature is well within the operational temperature of the PA12 under a vacuum bag cure, however with many resin systems using 176 °C cures the PA12 would not be a viable core material. The full

crystallization enthalpy was found to be 70 J/g for PA12.⁸⁹ Using the full crystallization enthalpy the crystallization fraction can be calculated to 88%. A high percent crystallinity fraction shows that the PA12 has time to equilibrate, meaning, the PA12 is not quench cooled, which can result in significant residual stresses. The PA12 percent crystallinity of 54% was also calculated.

4.2 Tensile Tests

With composition and thermal properties characterized it is important to evaluate the mechanical properties of the 3D printed structure. The mechanical properties of the 3D printed structure are significantly impacted by printing process. Moreover, the addition of fillers can improve a wide variety of characteristics. Wang's research showed the addition of carbon platelets to the PA12 allowed better heat conduction through the material and improved the stiffness. An addition of 5 wt% carbon increased the tensile strength while an increase of 7.5 wt % increased the stiffness.⁹⁰

One of the largest impacts of the manufacturing method is mechanical anisotropy. Mechanical anisotropy is very low for SLS, Polyjet, and printing based systems about ~2%.⁹¹ Factors that affect the mechanical property of these parts include annealing under different temperatures^{92,93}, layer thickness^{94,95}, part orientation⁹⁶⁻⁹⁹, feedstock uniformity, microstructure evolution, and the ability to form parts without thermal degradation of the powder.¹⁰⁰ Also, layer thickness, refresh rate, part bed temperature and hatch pattern also affect the mechanical properties.¹⁰¹ The use of virgin and recycled powders affects the mechanical properties of components as well.^{69,102} The reason why the listed systems have relatively low anisotropy is because the local volume is more densely packed by printed liquids, and these systems have lower sintering energies causing a

more uniform heating cycle. Because of the anisotropy that can occur within 3D printed structures it is important to characterize the strengths in the principle directions in which they were printed.

ASTM standards have been widely used by researchers to characterize mechanical properties of 3D printed parts. ASTM D638, which characterizes the tensile properties, has been followed by most research groups.^{103–106} Others have also followed ASTM D3039 due to premature failure within the radius of the of the dumbbell for ASTM 638.^{103,104} It is common practice to characterize the yield strength, ultimate strength, elasticity, and percent elongation at break. There is little literature regarding the mechanical properties of polymer materials manufactured using printing-based techniques. It is noted post processing techniques further improve the mechanical properties of printing-based 3D printing include post heating the powder further and adding a secondary material. Both these methods significantly reduce void content, which are present with this printing system. Using the later postprocessing technique, it was noticed that the addition of epoxy as an infiltrate generated the strongest parts and longer curing time increased the strength of the part.¹⁰⁷

The printing system used for this study uses a method similar to printing-based technologies but uses the addition of carbon platelets to increase the thermal conduction through the material. This process further sinter the powder particles together providing stronger parts with lower void content. The printer maintains very quick printing speeds and high part tolerance due the high accuracy of the printer array used. For the application as a core structure the anisotropy of the material needs to be characterized. Anisotropy exists within modern honeycomb core structures which have an W and L direction for different mechanical properties. As commonly used by other research ASTM D638 was used to characterize the mechanical properties in the two

principle directions the X and Y of the printer which sandwich structures will be manufactured in. The Z wasn't tested due to it being a material intensive process.

4.2.1 Experimental Setup

The tensile test specimens used ASTM D638 type I specimen. ASTM D638 is commonly used to measure orthotropic material properties throughout the literature. The specimen used the traditional dumbbell geometry with a thickness of $4 \pm .001 \text{ mm}$ and width of $13 \pm .0005 \text{ mm}$. 20 specimens were generated with 10 specimens in each longitudinal direction, the X and Y direction with reference to the printer. The large sample size is due to the high variability of 3D printed parts in order to reduce the beta error. Samples were designed using SolidWorks computer aided design. A HP Jet Fusion 4200 commercial grade printer was used to generate the samples. Samples were then processed using HP's 4200 series processing station shown in Figure 4.5. The thickness and width of the specimens were measured at three different points along the test specimen to the nearest 0.025 mm .



Figure 4.5: RapidMade's 4200 series processing station for HP's PA12 parts which recycles un used PA12 and results in high tolerance parts.

Tensile tests were conducted using Instron's universal testing system. The elongation rate was $5 \text{ mm}/\text{min}$ at a temperature of $23 \pm 2^\circ\text{C}$. For measuring the modulus of the specimens, a 2600 Instron extensometer was used, with a gauge length of 50 mm and max operational extension of 50 % for specific use with rigid plastics, composites, and metals testing. The strain gauge was removed at 1.5 kN for the X direction samples and 1 kN for Y direction samples. The strain gauge removed at different extensions due to the PA12 failing at a lower tensile strength than the X direction, avoiding damage to the strain gauge. The experimental setup can be seen in Figure 4.6 with the loaded specimen, grips measured to 115 mm and the strain gauge applied to the PA12 sample.



Figure 4.6: Experimental setup for tensile tests of PA12 samples in the Instron

Blue Hill was used to control the Instron and collect data which was then processed in MATLAB. The Modulus, percent yield, percent elongation at yield, ultimate tensile strength, total percent elongation, and energy absorption were evaluated for the two directions. The

confidence interval is determined by using a t-distribution as described earlier. With 9 degrees of freedom the t value 2.62 for a sample size of 10.

4.2.2 Results

A typical set of stress-strain plots are shown for the two different principal directions. The plot clearly shows the primary linear region, a singular yield stress and final failure. When results are plotted on the same plot it is clear that the material exhibits the same mechanical however after the yield point the X direction exhibits a significant increase in ultimate strain than the Y as shown in Figure 4.7.

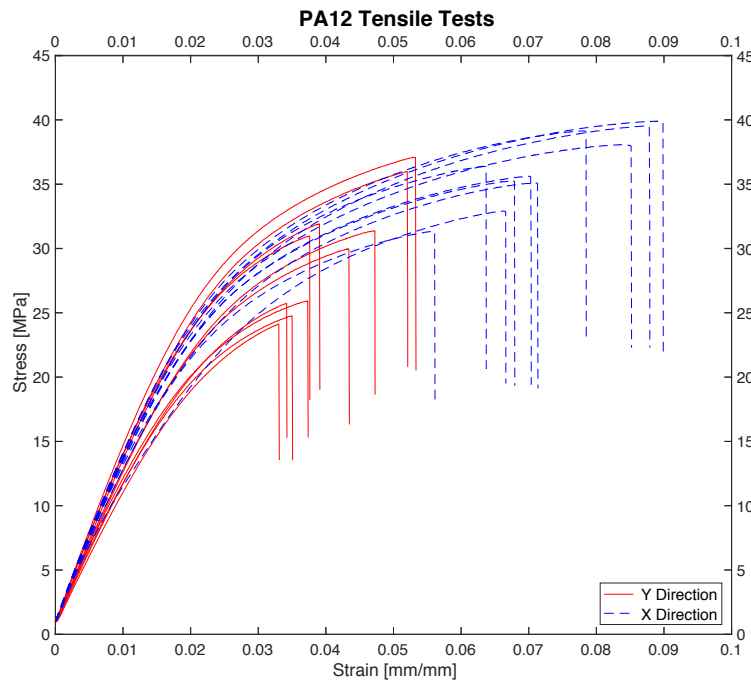


Figure 4.7: Graph of both the X and Y direction comparing the stress and strain. As shown, the X direction and Y direction have similar mechanical properties in the linear region and the ultimate tensile strengths

The mechanical properties were evaluated as shown in Table 4.3. The modulus of elasticity of the specimens were measured by the extensometer and had a mean about 1.5 GPa. The yield strength used a 0.2 % offset and was measured using the gantry system of the Instron. The mean yield stress was 23.3 MPa, with a percent elongation of about 1.79%. The ultimate tensile

strengths of the two directions differed by a small margin when comparing the confidence intervals of the two values. The ultimate tensile strength between the two directions are similar with the means only varying by 18% the X direction being $36.3 \pm 2 \text{ MPa}$ and in the Y direction being $29.8 \pm 3.3 \text{ MPa}$. However, the ultimate strain is differing significantly with the means differing by 44%.

Table 4.3: Shows the mechanical properties of the 3D printed specimens based on the direction they were printed and the statistical evaluation of the results.

Mechanical Property	Mean	Standard Deviation	95 % Confidence Interval
Modulus of Elasticity [GPa]			
<i>X Direction</i>	1.57	0.076	1.51 – 1.62
<i>Y Direction</i>	1.50	0.17	1.38 – 1.62
Yield Strength [MPa]			
<i>X Direction</i>	23.6	3.6	21.1 – 26.2
<i>Y Direction</i>	23.0	2.9	20.9 – 25.0
Percent Elongation at Yield [%]			
<i>X Direction</i>	1.72	0.25	1.54 – 1.90
<i>Y Direction</i>	1.74	0.17	1.62 – 1.86
Ultimate Tensile Strength [MPa]			
<i>X Direction</i>	36.3	2.9	34.3 – 38.4
<i>Y Direction</i>	29.8	4.6	26.5 – 33.1
Percent Elongation at Ultimate Tensile Strength [%]			
<i>X Direction</i>	7.38	0.78	6.58– 8.18
<i>Y Direction</i>	4.13	0.51	3.60 – 4.66
Modulus of Toughness [MJ/m³]			
<i>X Direction</i>	2.00	0.49	1.64 - 2.35
<i>Y Direction</i>	0.84	0.31	0.62 – 1.058

All samples exhibited a brittle fracture within the narrow section of the specimen, and often resulted in subsequent pieces breaking off at the fracture point as exhibited in Figure 4.8. With the increase in strain and stress the X direction absorbed 2.4 times more energy than the Y direction. The anisotropy of the material, although minimized by the printing method can be attributed to the density of powder bed when deposited before printing.

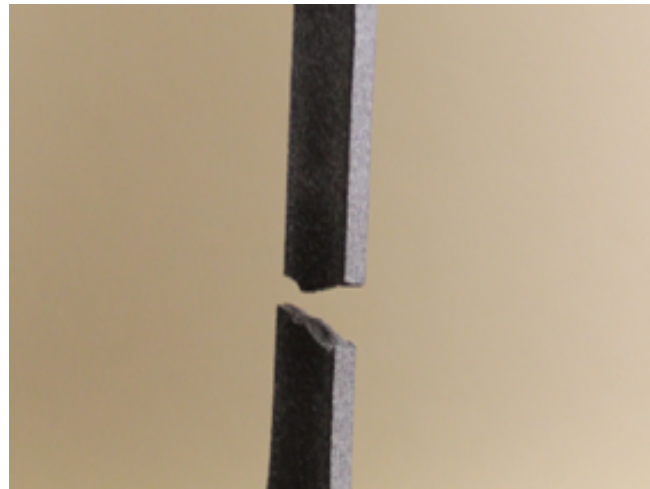


Figure 4.8: An example of how the PA12 samples fractured during testing. The fractures were very brittle and resulted in material breaking off the sample.

For applications with composites many core systems have a W and L direction showing orthotropic mechanical characteristics. Using the 3D printed core material, the longitudinal direction of the part or higher load section should be printed with the maximum load vector in the X direction to maximize performance.

4.3 Double Lap Joint Tests

Practical engineering has three basic methods for assembly and joining engineering components: mechanical joints, physical joints, and chemical joints. Adhesive joints have grown in popularity due to their ability to create lightweight, cost-effective, and integrated structures providing a uniform load distribution and higher damage tolerance. Composite sandwich panels rely on strong adhesive joints for optimal performance of the structure with fibers, core and adhesive all interacting with each other. Lap joints are commonly used to in composite sandwich panels and because of their simple loading conditions they can be used to determine the joint strength. This

technique is widely used by researchers to study stress distributions and failure mechanisms of adhesive bonding. The strength of the joint is largely dependent on the adhered and adhesive.

The investigation of damage onset to sandwich panels is comprised of damage initiation modes, which for mode: i) consist of core buckling, and core crushing ii) delamination in or along the facesheet and core iii) matrix cracking in facesheet iv) fiber breakage in facesheet. Delamination and debonding between facesheets and core are the most common initiation mode in composites sandwich panels

The double lap shear adhesive joints test or ASTM D3528-96 determines the tensile shear strengths of adhesives for bonded materials. The specimens only see pure shear and no peeling loads allowing the bond strength of the PA12 core to the composite facesheets to be determined. The bond strength is especially important as it is the primary failure initiation mode for composites laminates. The bond strength is a concern because the PA12 absorbs water from the atmosphere which adversely affects the bond strength. Conducting the double lap shear test will evaluate the bond strength and determine if the current process used can be applied. Also, homogenous nylon polymer blends are known to interact with epoxy as a nucleation site allowing for strong adhesion characteristics between the two materials. The resulting bond will provide a stronger interfacial strength when using an epoxy to bond the core to the skins.¹⁰⁸⁻¹¹¹

4.3.1 Experimental Setup

Three different specimens were generated using ASTM D3528-96 type B specimen geometry. The specimens were cured at 121°C, 132°C with vacuum and 132°C without vacuum. The specimens were made from the carbon fiber laminate, PA12, and epoxy film adhesive. The laminates were generated using Toray T700 unidirectional prepreg with their 2510 resin system.

Commonly used in aerospace applications allowing for flexible, out of auto clave, cures with high temperature resistance. The PA12 is manufactured by RapidMade using the same settings as the PA12 tensile samples. The film adhesive is a modified epoxy used for structural bonds requiring toughness and environmental resistance with the ability to cure at low temperatures. All the materials followed the tolerance of the ASTM D3528-96 with a thickness of $4 \text{ mm} \pm 0.125 \text{ mm}$ and an overlap thickness (L) of $12.7 \text{ mm} \pm 0.25 \text{ mm}$ Figure 4.9. The samples vary from the ASTM D3528-96 in that the sample width was 19 mm rather than 25 mm . The composite laminates are the sections placed in the grips due to their superior strength and stiffness compared to the PA12. The laminates consisted of 8 plies using a quasi-isotropic layup of $[0/\pm 45/90]_s$. The PA12 is then bonded to the carbon using the epoxy film adhesive to join them, causing a pure shear joint.

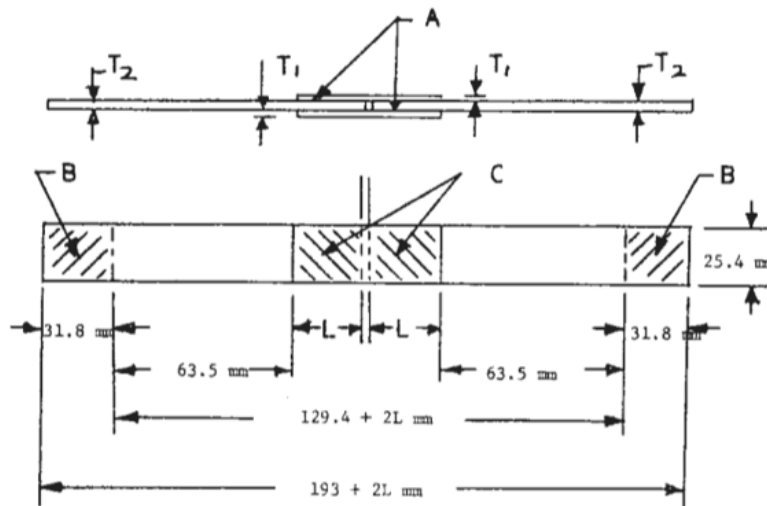


Figure 4.9: Experimental dimensions for double lap joint test (ASTM D 3528)

The samples were manufactured in a manner to reduce manufacturing time while maximizing bond strength of the joint. A REN Shape mold was CNC to the specifications of the sample geometry to allow the samples to be manufactured, Figure 4.10. All the plies were then cut accurately using the ply cutter providing repeatability within 0.13 mm . Plies were layed-up on the mold uncured with film adhesive and PA12 sections. The PA12 parts were unprocessed using

the initial print's surface finish. The hold time during the cure cycle was held for 5 hours. The vacuum provided a pressure of $.03 \pm 0.90 \text{ atm}$. The cure cycle specified for the for prepreg is 121°C , 132°C and the film adhesive is cured at 121°C .



Figure 4.10: Manufacturing process using a Renshape mold to layup on and vacuum bag to get compaction of the prepreg material.

Once the samples were cured, they were tested in tension using the clamps shown in Figure 4.11, as specified by the ASTM standard. Tests were conducted at room temperature, $23 \pm 2^\circ\text{C}$ and at humidity within the $50 \pm 5\%$. The grips used a 154 mm separation and pulled in tension at a displacement rate of $1.27 \text{ mm}/\text{min}$. Specimens were then tested until failure.

Data was further processed using MATLAB scripts to determine ultimate failure and the energy absorption. Similar to the tensile tests the t-test was used to determine the confidence interval of the three datasets. Even though a different population size was used for the 121°C cuew the confidence intervals are comparable due to a similar variance.



Figure 4.11: Double lap joint sample mounted in the Instron

4.3.2 Results

Typical set of stress versus strain curves for the double lap joint samples are shown in Figure 4.12 A through C. The stress strain curves exhibit two linear stages existing from 0 to 0.2% strain and 0.2% to failure. The initial stage indicates the film adhesive bridging the 2mm gap during the curing process. After the yielding of the epoxy film adhesive, the second linear behavior is exhibited by the PA12 being loaded due through the adhesive joint. Sample 6 and 10 showed very short first stage linear relationship.

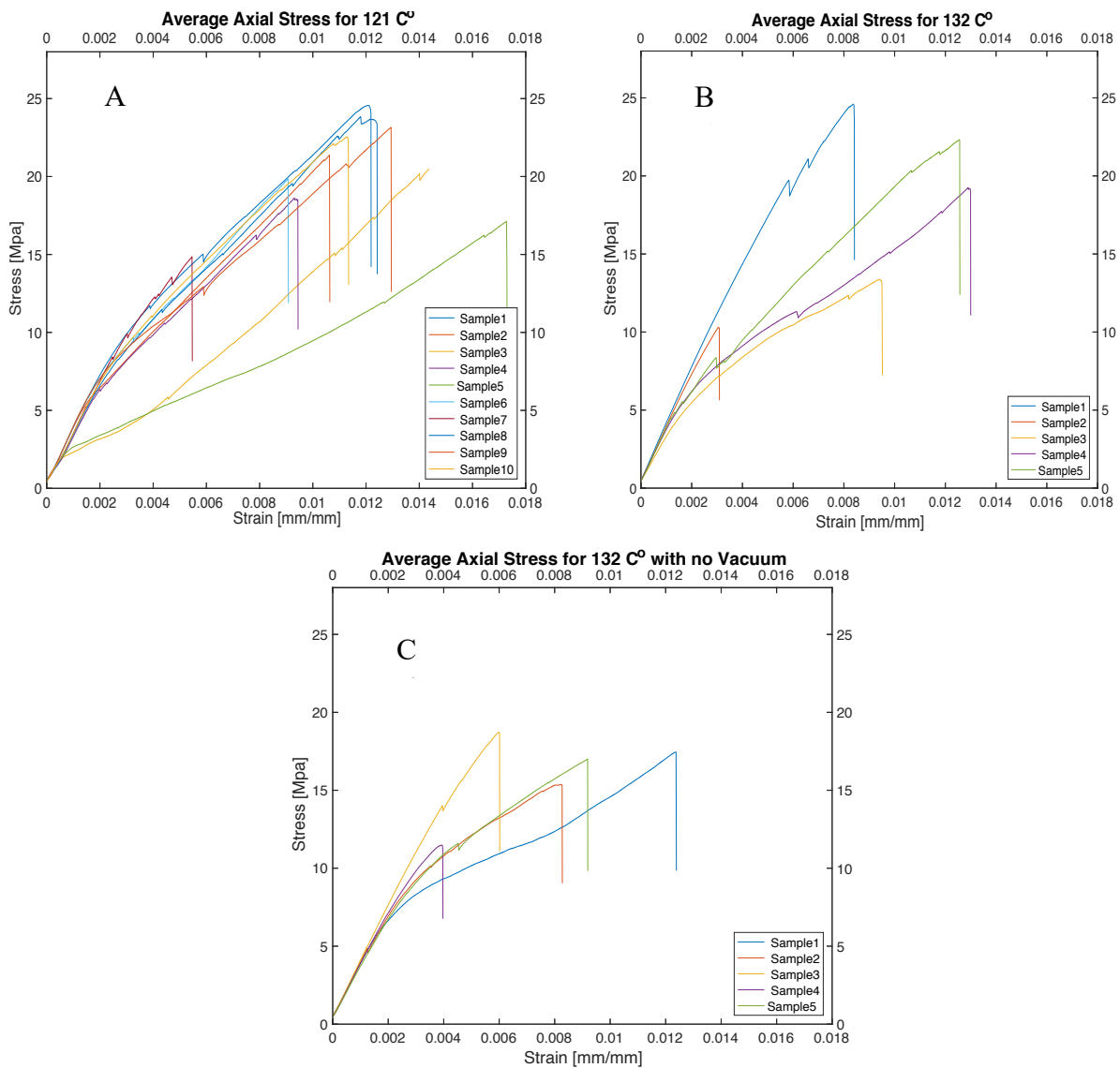


Figure 4.12: Average axial stress within the PA12 A) bonded at a 121°C cure with vacuum B) bonded at a 130°C cure with vacuum C) bonded at a 130°C cure with no vacuum

As shown in the Table 4.4, the ultimate yield strength was the highest in the 121°C degree cure samples showing a higher of 20.6 MPa mean. The 121°C degree cure has better bonding characteristics than the 130°C showed larger standard deviation and slightly lower average ultimate strength. The no vacuum cure showed similar ultimate strain properties although had a much lower ultimate strength resulting in a poor interfacial strength between the material. Modulus of Toughness or energy absorption to failure was the highest in the 121 °C at 135 kJ/m^3 than the 105 and 80.7 kJ/m^3 of the 132 °C cure with and without vacuum.

Table 4.4: Mechanical properties of the double lap joint specimens using the three different cure process.

Curing Process	Ultimate axial Stress [MPa]	Ultimate Strain [%]	Modulus of Toughness [kJ/m³]
121 °C degree cure	20.6 ± 1.84	1.15 ± 0.20	135 ± 24
132 °C degree cure	17.9 ± 5.79	0.93 ± 0.38	105.8 ± 55.7
132 °C degree cure (No vacuum)	16 ± 2.67	0.80 ± 0.30	80.7 ± 37.6

Meaning the 121 °C cure could absorb 22% more energy than the 132 °C with vacuum and 40.2% more energy than the cure without vacuum. All failures occurred along the PA12 samples at the gap between the two carbon samples, as shown in Figure 4.13.

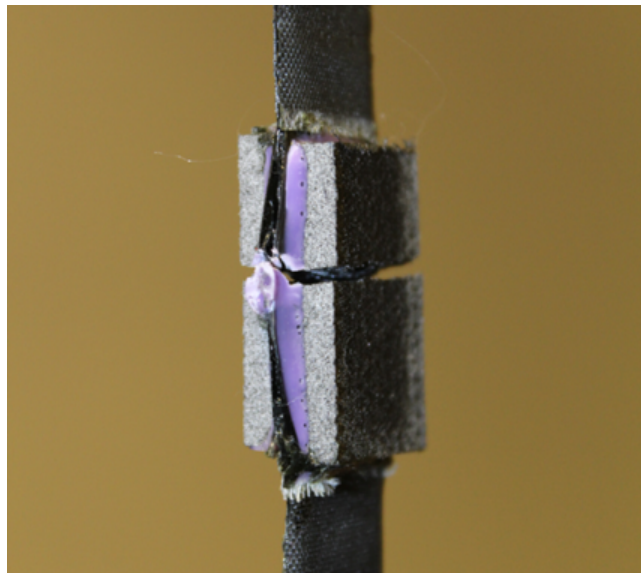


Figure 4.13: Fractured double lap joint specimen with a 250 cure and 1 atmosphere of vacuum pressure.

Additionally, the resin permeates well into the porous PA12 structure, even at to the lower temperatures. Showing the epoxy film adhesive was not adversely affected by the volatile content of the PA12, generating strong adhesion between the PA12 part and the carbon Figure 4.14. The lower temperature cure is preferred, as it reduces residual stresses from the difference in CTE of the PA12.

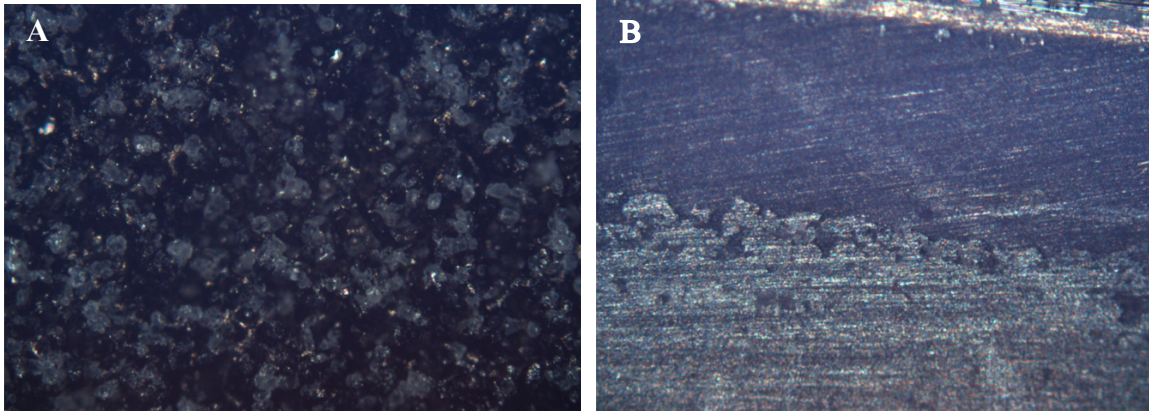


Figure 4.14: A) The porous surface finish of the PA12 using 10X objective lens. B) The bond interface between the epoxy resin system and the PA12 showing diffusion at the surface using a 10X objective lens.

5. Summary and Conclusion

In summary, this research developed efficient new models for the advancement of an AWES and a new rapid prototyping technique. The numerical model developed during this work was applied to two aircraft geometries, evaluating the energy loss due to tether drag, and includes a new model to simulate the effects of a bridle on pitch stability. In addition to the numerical model, a wind tunnel study was conducted on the delta wing geometry, to explore aerodynamic performance at extremely high angles of attack. The second part of the work is focused on characterizing a new composites manufacturing method which involves a 3D printed core structure, allowing faster prototyping of a number of different geometries to be tested.

The accuracy of the aerodynamic model was verified at low AOA comparing the simulated results to the wind tunnel tests with an 11% error. The error is largely attributed to difference in the model not being able to model turbulent flow. The power generation code was validated by showing similar results to previous power generation models. An ASK 21 geometry generated significantly higher power than the delta wing emphasizing that a high coefficient of lift to drag ratio $\frac{C_L}{C_D}$ is critical for optimal power generation of an AWES. The high coefficient of lift to drag ratio also has a large effect at lower wind velocities. Additionally, typical tether drag reduces the efficiency to 34% of the optimal efficiency. Further development of more efficient AWES relies on strong, light weight, and low drag tethers. Simulation of a bridal showed significant increase of static pitch stability allowing the horizontal stabilizer size to be reduced. The forward tether helps significantly stabilize with offset from the CG and large angles. Where the aft bridal can adjust the instability of the aircraft based on its angle and distance from the CG. Additionally, with the large tensile loads transferred to the bridal from the tether, the aerodynamic pitching moments can be easily dominated by the moments induced by the bridal. The bridal aids in adding stability to the aircraft which wouldn't be otherwise possible due to the difficulty of mounting the tether directly to the CG of the AWES.

The delta wing geometry also demonstrated delayed stall compared to traditional wing configurations used on wind energy applications and exhibited high coefficients of lift at extreme angles of attack. These characteristics are attributed to strong wing tip vortices generated by the dihedral section of the wing which delays separation of the flow across the wing. High AOA lift allows the aircraft to take off at extremely steep angles with significant tether tension values during takeoff. High tension translates into early control of the aircraft during takeoff and ability to generate energy at short tether lengths increasing the energy generation. Such a geometry

would be ideal for smaller energy generation applications in rural areas where the investment of a sophisticated launch system is not desirable.

In addition, PA12 and carbon fiber reinforced polymers (CFRP) were used to thermally and mechanically characterize a new composite manufacturing method, potentially applicable to AWES. The results of the thermal gravimetric analysis (TGA) revealed the composition of the PA12 after the 3D printing process to be 1.5 % water, 82% PA12, and 14 % carbon platelets. The presence of water can adversely affect the bond strength between the PA12 and carbon, which was the motivation behind the double lap joint test. With a large weight percent of carbon platelets being added to the final part, the 3D printed part can be expected to have a higher tensile strength, and Young's modulus making it ideal for composite manufacturing applications.⁹⁰ The PA12 part analyzed using Differential Scanning Calorimetry, allows the thermal and semi crystalline properties of the PA12 to be determined. With a melting temperature of 177.9 °C for the PA12 and a maximum cure temperature of 132 °C for the CFRP, the PA12 can withstand the temperatures during cure cycle. The PA12 also exhibits a high percent crystallinity at 54%. The high percent crystallinity provides preferential mechanical properties.¹¹² Also, because there is a high degree of crystallinity, there are little residual stresses within the 3D printed part from processing.

In addition to the thermal characterization of the PA12, the mechanical properties of the 3D printed structure were also evaluated in the two principal directions X and Y of the 3D printer. The X direction had the longitudinal tensile test sample oriented along the front of the printer with the Y direction oriented into the depth of the printer. Within the elastic region of the tensile tests the mechanical properties are well within each other confidence intervals and exhibit the same Young's modulus for the X and Y. However, anisotropy becomes evident during the

ultimate failure with the X direction exhibiting 18 % higher ultimate stress and 44% ultimate strain resulting in a 2.4 more energy absorption than the Y direction. Making the X direction the primary direction, which should be oriented appropriately for the loading condition. This anisotropy needs to be considered when designing the composite structure, much like the L and W direction of normal honeycomb material, to avoid premature failure of the core material.

A concern with using PA12 as a core structure is the strength of the adhesion between the composite material and the PA12 core, especially considering the 1.5% water content. The water showed no effect on the film adhesive which demonstrated good bonding characteristics with low porosity and good interface with the porous PA12 structure. Double lap joint test results exhibited failures in the PA12 at the lap joint without the adhesive failing, demonstrating a strong adhesion between the PA12 and the carbon. Additionally, out of the three curing process the lower temp 121°C cure showed the strongest adhesion with the mean modulus of toughness being 13% more than 132 °C cure with vacuum and 22% more than the 132°C cure with no vacuum. The difference is attributed to the lower residual stresses caused by the CTE mismatch at higher temperatures, and the reduction in compression without the vacuum making the lower cure temperatures the preferable manufacturing technique.

5.1 Future Work

This work covers new models and characterizes a rapid prototyping method. The next step for the development of AWES is more in-depth wind tunnel testing, structural and control analyses. These developments will provide more accurate This Validation of the power generation and bridal model need to be conducted. Furthermore, the power generation model is optimistic because it does not account for dynamic effects. Computational fluid analysis which takes into

account turbulent flow should be conducted to provide more accurate power generation results. Additional, wind tunnel testing needs to be conducted to validate the pitch stability equation derived with roll fixed for the aircraft. Once a large, efficient wing prototype is developed, full scale testing should be conducted using rapid prototyped designs to validate and modify the power generation model. Before full scale AWES are prototyped, scaled testing should be conducted on the new composite manufacturing technique. Structural simulations using Finite Element Analysis FEA should be conducted to analyze how the core geometry affects the flexural stiffness, energy absorption, and strength of the sandwich structure. These simulations should be validated with physical tests as well. Once more about these structures are understood, through testing, the manufacturing technique should be implemented in full scale prototyping in combination with topography optimization to take full advantage of this manufacturing technique. Additionally, a cost analysis needs to be conducted determining the cost efficiency of this new manufacturing technique for AWES applications.

References

1. Wrigley EA. Energy and the English Industrial Revolution. *Philosophical Transactions of the Royal Society of London A: Mathematical, Physical and Engineering Sciences*. 2013;371(1986). doi:10.1098/rsta.2011.0568.
2. Melorose J, Perroy R, Careas S. Roadmap 2050 A practical guide to a prosperous low carbon Europe. *Statewide Agricultural Land Use Baseline 2015*. 2015;1. doi:10.1017/CBO9781107415324.004.
3. Peeringa J, Brood R, Ceyhan O, Engels W, de Winkel G, Winkel G De. Upwind 20MW Wind Turbine Pre-Design: Blade design and control. *ECN-E--11-017 December*. 2011;(December):1-53.
4. Berry D. Innovation and the price of wind energy in the US. *Energy Policy*. 2009;37(11):4493-4499.
5. Cherubini A, Papini A, Vertechy R, Fontana M. Airborne Wind Energy Systems: A review of the technologies. *Renewable and Sustainable Energy Reviews*. 2015;51:1461-1476. doi:10.1016/j.rser.2015.07.053.
6. Ahrens U, Diehl M, Schmehl R. *Airborne Wind Energy*. Springer Science & Business Media; 2013.
7. LOYD ML. Crosswind kite power (for large-scale wind power production). *Journal of Energy*. 1980;4(3):106-111. doi:10.2514/3.48021.
8. Diehl M. Airborne wind energy: Basic concepts and physical foundations. *Green Energy and Technology*. 2013:3-22. doi:10.1007/978-3-642-39965-7_1.
9. Fagiano L, Nguyen-Van E, Rager F, Schnez S, Ohler C. Autonomous Takeoff and Flight of a Tethered Aircraft for Airborne Wind Energy. *IEEE Transactions on Control Systems Technology*. 2018;26(1):151-166. doi:10.1109/TCST.2017.2661825.
10. Licitra G, Bürger A, Williams P, Ruiterkamp R, Diehl M. System Identification of a Rigid Wing Airborne Wind Energy System. 2017. <http://arxiv.org/abs/1711.10010>.
11. Power A. Our story – Ampyx Power B.V.
12. Makani. Journey. <https://x.company/makani/journey/>.
13. Mitton P. Altaeros. <http://www.altaeros.com/index.html>.
14. Canale M, Fagiano L, Ippolito M, Milanese M. Control of tethered airfoils for a new class of wind energy generator. *Proceedings of the 45th IEEE Conference on Decision and Control*. 2006:4020-4026. doi:10.1109/CDC.2006.376775.
15. Pocock G. *The Aeropleustic Art Or Navigation in the Air, by the Use of Kites Or Buoyant Sails*. Sherwood & Company; 1827.
16. De Lellis M, Mendonça AK, Saraiva R, Trofino A, Lezana. Electric power generation in wind farms with pumping kites: An economical analysis. *Renewable Energy*. 2016;86:163-172. doi:10.1016/j.renene.2015.08.002.
17. Roberts BW, Shepard DH. Unmanned rotorcraft to generate electricity using upper atmospheric winds. In: *Australian International Aerospace Congress*. ; 2003.
18. Bauer F, Kennel RM, Hackl CM, Campagnolo F, Patt M, Schmehl R. Drag power kite with very high lift coefficient. *Renewable Energy*. 2018;118:290-305. doi:10.1016/j.renene.2017.10.073.

19. Wellicome JF. Some comments on the relative merits of various wind propulsion devices. *Journal of Wind Engineering and Industrial Aerodynamics*. 1985;20(1-3):111-142. doi:10.1016/0167-6105(85)90015-7.
20. Diehl M, Hans BG, Schloder P. Johannes. A Real-Time Iteration Scheme for Nonlinear Optimization in Optimal Feedback Control. 2005;27(3):937-966.
21. Williams P, Lansdorp B, Ockels W. Optimal Trajectories for Tethered Kite Mounted on a Vertical Axis Generator. *AIAA Modelling and Simulation Technologies Conference and Exhibit*. 2007;AIAA 2007(20-23 August):6706. doi:doi:10.2514/6.2007-6706.
22. Argatov I, Rautakorpi P, Silvennoinen R. Estimation of the mechanical energy output of the kite wind generator. *Renewable Energy*. 2009;34(6):1525-1532. doi:10.1016/j.renene.2008.11.001.
23. Kim J, Park C. Wind power generation with a parawing on ships, a proposal. *Energy*. 2010;35(3):1425-1432. doi:10.1016/j.energy.2009.11.027.
24. Breukels J. *An Engineering Methodology for Kite Design.*; 2010. http://repository.tudelft.nl/assets/uuid:cdece38a-1f13-47cc-b277-ed64fdda7cdf/Thesis_jeroen_breukels.pdf <http://repository.tudelft.nl/view/ir/uuid:cdece38a-1f13-47cc-b277-ed64fdda7cdf/>.
25. Miller LM, Gans F, Kleidon A. Jet stream wind power as a renewable energy resource: Little power, big impacts. *Earth System Dynamics*. 2011;2(2):201-212. doi:10.5194/esd-2-201-2011.
26. Dadd GM, Hudson DA, Sheno RA. Determination of kite forces using three-dimensional flight trajectories for ship propulsion. *Renewable Energy*. 2011;36(10):2667-2678. doi:10.1016/j.renene.2011.01.027.
27. Argatov I, Rautakorpi P, Silvennoinen R. Apparent wind load effects on the tether of a kite power generator. *Journal of Wind Engineering and Industrial Aerodynamics*. 2011;99(10):1079-1088. doi:10.1016/j.jweia.2011.07.010.
28. Haug S. Design of a Kite Launch and Retrieval System. 2012;(October).
29. Lozano RJ, Alamir M, Dumon J, Hably A. *Control of a Wind Power System Based on a Tethered Wing*. Vol 45. IFAC; 2012. doi:10.3182/20120213-3-IN-4034.00027.
30. Goldstein L. Theoretical analysis of an airborne wind energy conversion system with a ground generator and fast motion transfer. *Energy*. 2013;55:987-995. doi:10.1016/j.energy.2013.03.087.
31. Costello S, François G, Bonvin D. Real-time optimization for kites. *IFAC Proceedings Volumes (IFAC-PapersOnline)*. 2013;5(PART 1):64-69. doi:10.3182/20130703-3-FR-4039.00004.
32. Castellani F, Garinei A. On the way to harness high-altitude wind power: Defining the operational asset for an airship wind generator. *Applied Energy*. 2013;112:592-600. doi:10.1016/j.apenergy.2013.01.019.
33. Coleman J, Ahmad H, Pican E, Toal D. Modelling of a synchronous offshore pumping mode airborne wind energy farm. *Energy*. 2014;71:569-578. doi:10.1016/j.energy.2014.04.110.
34. Archer CL, Delle Monache L, Rife DL. Airborne wind energy: Optimal locations and variability. *Renewable Energy*. 2014;64:180-186. doi:10.1016/j.renene.2013.10.044.
35. Zanon M, Gros S, Meyers J, Diehl M. Airborne wind energy: Airfoil-airmass interaction. *IFAC Proceedings Volumes (IFAC-PapersOnline)*. 2014;19(2013):5814-5819. doi:10.3182/20140824-6-ZA-1003.00258.
36. Erhard M, Strauch H. Flight control of tethered kites in autonomous pumping cycles for airborne wind energy. *Control Engineering Practice*. 2015;40:13-26. doi:10.1016/j.conengprac.2015.03.001.

37. Fechner U, van der Vlugt R, Schreuder E, Schmehl R. Dynamic model of a pumping kite power system. *Renewable Energy*. 2015;83:705-716. doi:10.1016/j.renene.2015.04.028.
38. Heilmann JN. The technical and economic potential of airborne wind energy. 2012.
39. Cherubini A, Vertechy R, Fontana M. Simplified model of offshore Airborne Wind Energy Converters. *Renewable Energy*. 2016;88:465-473. doi:10.1016/j.renene.2015.11.063.
40. Argatov I, Shafranov V. Economic assessment of small-scale kite wind generators. *Renewable Energy*. 2016;89:125-134. doi:10.1016/j.renene.2015.12.020.
41. Fagiano L, Schnez S. On the take-off of airborne wind energy systems based on rigid wings. *Renewable Energy*. 2017;107:473-488. doi:10.1016/j.renene.2017.02.023.
42. Deng Y. Title CARBON FIBER ELECTRONIC INTERCONNECTS. 2007.
<http://drum.lib.umd.edu/handle/1903/6997>
<http://drum.lib.umd.edu/bitstream/handle/1903/6997/umi-umd-4508.pdf?sequence=1>.
43. Bakis CE, Bank LC, Brown VI, et al. Fiber-reinforced polymer composites for construction—State-of-the-art review. *Journal of composites for construction*. 2002;6(2):73-87.
44. Games S. Method and apparatus for making glass wool. October 1938.
45. Carleton E. Glycol-maleic acid resin and process of making same. March 1940.
46. Gibson RF. *Principles of Composite Material Mechanics*. CRC press; 2011.
47. Reissner E. Finite deflections of sandwich plates. *Journal of the Aeronautical Sciences*. 1948;15(7):435-440.
48. Bacon R. Growth, structure, and properties of graphite whiskers. *Journal of Applied Physics*. 1960;31(2):283-290. doi:10.1063/1.1735559.
49. Robert S. Glass fiber-resin composite product. June 1950.
50. Shindo A. 130. On the carbonization of polyacrylonitrile fiber. *Carbon*. 1964;1(3):391-392.
51. Otani S, Yokoyama A. Characteristic Chemical Constitution of Pitch Materials Suitable for the MP Carbon Fiber. *Bulletin of the Chemical Society of Japan*. 1969;42(5):1417-1424.
52. Freeman WT, Campbell MD. Thermal expansion characteristics of graphite-reinforced composite materials. In: *2. Conference on Composite Materials: Testing and Design*. Hercules Inc., Cumberland, MD; 1972.
53. Sheikh-Ahmad JY. *Machining of Polymer Composites*. Springer; 2009.
54. Pinter WH, Smith DE. Method of winding a wind turbine blade using a filament reinforced mandrel. December 1980.
55. Griffee Jr DG, Gruska Jr CJ. Composite wind turbine blade. January 1981.
56. Johnston JF, Farone WA, Mikhail A. Composite wind turbine rotor blade and method for making same. December 1990.
57. Iijima S. Helical microtubules of graphitic carbon. *Nature*. 1991;354:56.
<http://dx.doi.org/10.1038/354056a0>.
58. Salvetat J-P, Bonard J-M, Thomson NH. Mechanical properties of carbon nanotubes. *Applied Physics A*. 1999;69(3):255-260. doi:10.1007/s003390050999.
59. Kodama H. Automatic method for fabricating a three-dimensional plastic model with photo-hardening polymer. *Review of Scientific Instruments*. 1981;52(11):1770-1773.
doi:10.1063/1.1136492.

60. André JC, Le Mehaute A, De Witte O. Dispositif pour réaliser un modèle de pièce industrielle. *French patent*. 1984;84(11):241.
61. Hull CW. Apparatus for production of three-dimensional objects by stereolithography. March 1986.
62. Crump SS. Apparatus and method for creating three-dimensional objects. June 1992.
63. Kruth JP, Leu MC, Nakagawa T. Progress in additive manufacturing and rapid prototyping. *CIRP Annals - Manufacturing Technology*. 1998;47(2):525-540. doi:10.1016/S0007-8506(07)63240-5.
64. Sachs EM, Haggerty JS, Cima MJ, Williams PA. Three-dimensional printing techniques. April 1993.
65. Kruth J-P, Leu M-C, Nakagawa T. Progress in additive manufacturing and rapid prototyping. *Cirp Annals*. 1998;47(2):525-540.
66. Kumar S, Kruth JP. Composites by rapid prototyping technology. *Materials and Design*. 2010;31(2):850-856. doi:10.1016/j.matdes.2009.07.045.
67. Mironov V, Boland T, Trusk T, Forgacs G, Markwald RR. Organ printing: Computer-aided jet-based 3D tissue engineering. *Trends in Biotechnology*. 2003;21(4):157-161. doi:10.1016/S0167-7799(03)00033-7.
68. Cheng J, Lao S, Nguyen K, Ho W, Cummings A, Koo J. SLS Processing Studies of Nylon 11 Nanocomposites. *Proceedings of the Solid Freeform Fabrication Symposium, Austin, Texas*. 2005;(June):141-149.
<http://utwirend.engr.utexas.edu/lff/symposium/proceedingsArchive/pubs/Manuscripts/2005/2005-13-Cheng.pdf>.
69. Zarringhalam H, Hopkinson N, Kamperman NF, de Vlieger JJ. Effects of processing on microstructure and properties of SLS Nylon 12. *Materials Science and Engineering A*. 2006;435-436:172-180. doi:10.1016/j.msea.2006.07.084.
70. Ning F, Cong W, Qiu J, Wei J, Wang S. Additive manufacturing of carbon fiber reinforced thermoplastic composites using fused deposition modeling. *Composites Part B: Engineering*. 2015;80:369-378. doi:10.1016/j.compositesb.2015.06.013.
71. The amazing science behind HP's new full-color 3D printers.
72. Karalekas DE. Study of the mechanical properties of nonwoven fibre mat reinforced photopolymers used in rapid prototyping. *Materials & Design*. 2003;24(8):665-670. doi:https://doi.org/10.1016/S0261-3069(03)00153-5.
73. Gupta A, Ogale AA. Dual curing of carbon fiber reinforced photoresins for rapid prototyping. *Polymer Composites*. 2002;23(6):1162-1170. doi:10.1002/pc.10509.
74. Li N, Li Y, Liu S. Rapid prototyping of continuous carbon fiber reinforced polylactic acid composites by 3D printing. *Journal of Materials Processing Technology*. 2016;238:218-225. doi:10.1016/j.jmatprotec.2016.07.025.
75. Yao X, Luan C, Zhang D, Lan L, Fu J. Evaluation of carbon fiber-embedded 3D printed structures for strengthening and structural-health monitoring. *Materials and Design*. 2017;114:424-432. doi:10.1016/j.matdes.2016.10.078.
76. Li T, Wang L. Bending behavior of sandwich composite structures with tunable 3D-printed core materials. *Composite Structures*. 2017;175:46-57. doi:10.1016/j.compstruct.2017.05.001.
77. Hao W, Liu Y, Zhou H, Chen H, Fang D. Preparation and characterization of 3D printed continuous carbon fiber reinforced thermosetting composites. *Polymer Testing*. 2018;65(September 2017):29-34. doi:10.1016/j.polymertesting.2017.11.004.

78. Melin T. User's guide and reference manual for Tornado. *Royal Inst of Technology (KTH), Stockholm, Sweden*. 2000. <http://www.redhammer.se/tornado/manual.pdf>.
79. DeYoung J. Historical Evolution of Vortex-Lattice Methods. *Langley Research Center*. 2018.
80. Anderson JD. *Fundamentals of Aerodynamics*. McGraw-Hill Companies; 1984.
81. Kroo I. *Applied Aerodynamics: A Digital Textbook*. Desktop, Aeronautics; 1997.
82. Melin T. Using Internet interactions in developing vortex lattice software for conceptual design Using Internet Interactions in Developing Vortex Lattice Software for Conceptual Design Tomas Melin. 2003;(December 2003).
https://www.researchgate.net/profile/Tomas_Melin/publication/260198739_Using_Internet_interactions_in_developing_vortex_lattice_software_for_conceptual_design/links/5a02ed59458515713b3eaf12/Using-Internet-interactions-in-developing-vortex-lattice-software.
83. Perkins CD, Hage RE. *Airplane Performance, Stability and Control*. Wiley; 1949.
<https://books.google.com/books?id=ZoLLtgEACAAJ>.
84. Moran J. *An Introduction to Theoretical and Computational Aerodynamics*. Courier Corporation; 2003.
85. Luckring JM. Some Recent Applications of the Suction Analogy to Asymmetric Flow Situations. Vortex-Lattice Utilization. NASA SP-405, 1976. *TABLE I-GEOMETRIC CHARACTERISTICS OF MODEL TABLE II-NOMINAL TUNNEL TEST CONDITIONS 00097 to 00268 00188 to 00407 00341 to 01307 Yaw Roll CONJIG O BVWCS D BVWC.:219-236*.
86. dll Version Ps. Schleicher ASK 21 two seat glider. 2003.
87. Sheldahl RE, Klimas PC. *Aerodynamic Characteristics of Seven Symmetrical Airfoil Sections through 180-Degree Angle of Attack for Use in Aerodynamic Analysis of Vertical Axis Wind Turbines*. Sandia National Labs., Albuquerque, NM (USA); 1981.
88. TORAY. 2510 Prepreg System. www.toraycma.com.
89. Plummer CJG, Zanetto JE, Bourban PE, Manson JAE. The crystallization kinetics of polyamide-12. *Colloid and Polymer Science*. 2001;279(4):312-322. doi:10.1007/s003960000425.
90. Wang Y, Rouholamin D, Davies R, Ghita OR. Powder characteristics, microstructure and properties of graphite platelet reinforced Poly Ether Ether Ketone composites in High Temperature Laser Sintering (HT-LS). *Materials & Design*. 2015;88:1310-1320.
91. Dizon JRC, Espera AH, Chen Q, Advincula RC. Mechanical characterization of 3D-printed polymers. *Additive Manufacturing*. 2018;20:44-67. doi:10.1016/j.addma.2017.12.002.
92. Manapat JZ, Mangadlao JD, Tiu BDB, Tritchler GC, Advincula RC. High-strength stereolithographic 3D printed nanocomposites: graphene oxide metastability. *ACS applied materials & interfaces*. 2017;9(11):10085-10093.
93. Zguris Z. How mechanical properties of stereolithography 3D prints are affected by UV curing. *Available online: formlabs com (accessed on 7 March 2017)*. 2016.
94. Chockalingam K, Jawahar N, Chandrasekhar U. Influence of layer thickness on mechanical properties in stereolithography. *Rapid Prototyping Journal*. 2006;12(2):106-113.
95. Chockalingam K, Jawahar N, Chandrasekar U, Ramanathan KN. Establishment of process model for part strength in stereolithography. *Journal of Materials Processing Technology*. 2008;208(1-3):348-365.
96. Ajoku U, Hopkinson N, Caine M. Experimental measurement and finite element modelling of the compressive properties of laser sintered Nylon-12. *Materials Science and Engineering: A*. 2006;428(1-2):211-216.

97. Ajoku U, Saleh N, Hopkinson N, Hague R, Erasenthiran P. Investigating mechanical anisotropy and end-of-vector effect in laser-sintered nylon parts. *Proceedings of the Institution of Mechanical Engineers, Part B: Journal of Engineering Manufacture*. 2006;220(7):1077-1086.
98. Caulfield B, McHugh PE, Lohfeld S. Dependence of mechanical properties of polyamide components on build parameters in the SLS process. *Journal of Materials Processing Technology*. 2007;182(1-3):477-488.
99. Kutz M. *Applied Plastics Engineering Handbook: Processing and Materials*. William Andrew; 2011.
100. Bourell DL, Watt TJ, Leigh DK, Fulcher B. Performance limitations in polymer laser sintering. *Physics Procedia*. 2014;56:147-156.
101. Jain PK, Pandey PM, Rao PVM. Experimental investigations for improving part strength in selective laser sintering. *Virtual and Physical Prototyping*. 2008;3(3):177-188.
102. Gornet TJ, Davis KR, Starr TL, Mulloy KM. Characterization of selective laser sintering materials to determine process stability. In: *Solid Freeform Fabrication Symposium*. ; 2002:546-553.
103. Ahn S-H, Montero M, Odell D, Roundy S, Wright PK. Anisotropic material properties of fused deposition modeling ABS. *Rapid prototyping journal*. 2002;8(4):248-257.
104. Letcher T, Waytashek M. Material property testing of 3D-printed specimen in PLA on an entry-level 3D printer. In: *ASME 2014 International Mechanical Engineering Congress and Exposition*. American Society of Mechanical Engineers; 2014:V02AT02A014-V02AT02A014.
105. Melenka GW, Cheung BKO, Schofield JS, Dawson MR, Carey JP. Evaluation and prediction of the tensile properties of continuous fiber-reinforced 3D printed structures. *Composite Structures*. 2016;153:866-875. doi:10.1016/j.compstruct.2016.07.018.
106. Cantrell JT, Rohde S, Damiani D, et al. Experimental characterization of the mechanical properties of 3D-printed ABS and polycarbonate parts. *Rapid Prototyping Journal*. 2017;23(4):811-824.
107. Impens D, Urbanic RJ. Assessing the impact of post-processing variables on tensile and compression characteristics for 3D printed components. *IFAC-PapersOnLine*. 2015;48(3):652-657.
108. Kim KW, Kim DK, Kim BS, et al. Cure behaviors and mechanical properties of carbon fiber-reinforced nylon6/epoxy blended matrix composites. *Composites Part B: Engineering*. 2017;112:15-21. doi:10.1016/j.compositesb.2016.12.009.
109. Zhong Z, Guo Q. Miscibility and cure kinetics of nylon/epoxy resin reactive blends. *Polymer*. 1998;39(15):3451-3458. doi:10.1016/S0032-3861(97)10237-3.
110. Peerman D, Tolberg W, Floyd D. Reaction of Polyamide Resins and Epoxy Resins. *Industrial & Engineering Chemistry*. 1957;49(7):1091-1094. doi:10.1021/ie50571a025.
111. Deng S, Djukic L, Paton R, Ye L. Thermoplastic-epoxy interactions and their potential applications in joining composite structures - A review. *Composites Part A: Applied Science and Manufacturing*. 2015;68:121-132. doi:10.1016/j.compositesa.2014.09.027.
112. McKeen LW, Massey LK. Permeability Properties of Plastics and Elastomers: A Guide to Packaging and Barrier Materials. *Permeability Properties of Plastics and Elastomers*. 2012:121-144. doi:10.1016/B978-1-4377-3469-0.10008-6.

Appendix

Appendix A: Derivation of pitch stability equation.

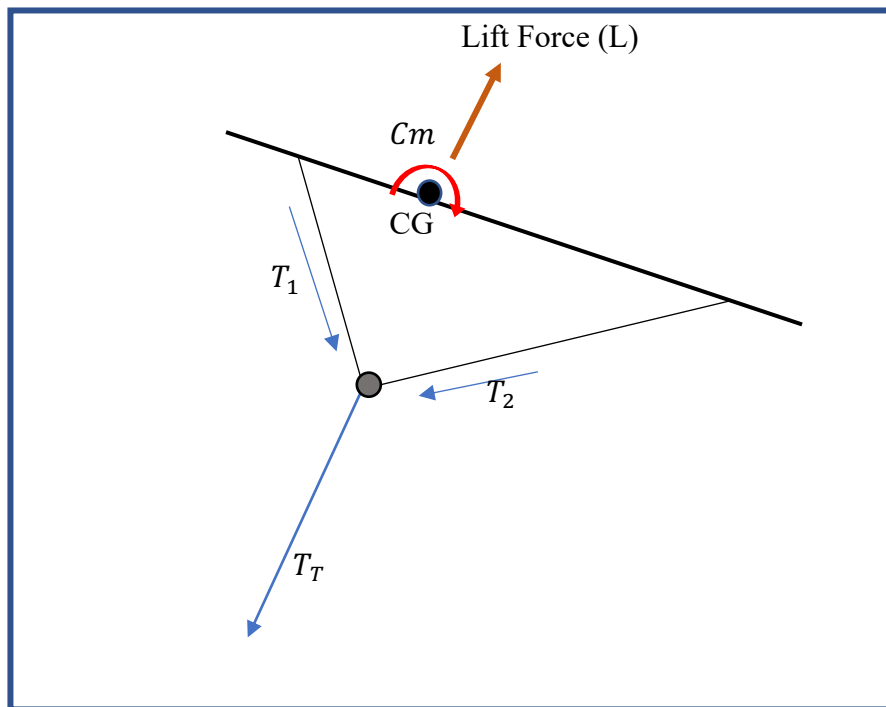
Resourced used: *Airplane Performance Stability and Control* by Perkins Hage.

Total Tension of the tether is equal to the lift force generated by the airfoil.

$$T_T = L$$

$$\sin(\theta_1) * T_1 + \sin(\theta_2) * T_2 = L \qquad \cos(\theta_1) * T_1 = \cos(\theta_2) * T_2$$

The moments controlling pitch are dominated by forces perpendicular to the air foil for the tether. Tension parallel to the airfoil are equal to have a forces balance at the intersection of the bridal. This is shown in the figure below.



(NOTE: If the tether mount is to the left of the CG then d is negative)

$$M_{te} = T_1 d_1 \sin(\theta_1) + T_2 d_2 \sin(\theta_2)$$

Sum of the moments about the CG:

$$M_{cg} = N x_a + C z_a + M_{ac} + \frac{M_{Fus}}{Nac} + M_{act} + C_t h_t - N_t l_t + M_{te}$$

Divide through by dynamic pressure (q), wing area (S_w), and the mean aerodynamic cord (c)
 $[q S_w c]$:

(NOTE: the ratio of $\frac{q_t}{q} = \eta$ the tail efficiency factor typical values range from 0.85-0.95)

$$C_{m_{cg}} = C_N \frac{x_a}{c} + C_c \frac{z_a}{c} + C_{mac} + C_{m_{FUS}} \frac{S_t c_t}{S_w c} \eta_t + C_{mact} \frac{S_t h_t}{S_w c} \eta_t - C_{Nt} \frac{S_t l_t}{S_w c} \eta_t + C_{T_1} \frac{d_1}{c} \sin(\theta_1) + C_{T_2} \frac{d_1}{c} \sin(\theta_2)$$

The fifth and sixth terms of the above equation have been found to be negligible when compared to other terms. $C_{m_{cg}}$ must equal zero to have equilibrium at that given flight condition:

$$C_{m_{cg}} = C_N \frac{x_a}{c} + C_c \frac{z_a}{c} + C_{mac} + C_{m_{FUS}} \frac{S_t l_t}{S_w c} \eta_t - C_{Nt} \frac{S_t l_t}{S_w c} \eta_t + C_{T_1} \frac{d_1}{c} \sin(\theta_1) + C_{T_2} \frac{d_1}{c} \sin(\theta_2)$$

For the aircraft to be stable the $C_{m_{cg}}$ with respect to C_L must be negative. The derivative of the with respect to C_L is applied to the equation above to determine the stability of the aircraft:

$$\frac{dC_m}{dC_L} = \frac{dC_N}{dC_L} \frac{x_a}{c} + \frac{dC_c}{dC_L} \frac{z_a}{c} + \frac{dC_{mac}}{dC_L} + \left(\frac{dC_m}{dC_L} \right)_{FUS} \frac{S_t c_t}{S_w c} \eta_t - \frac{dC_{Nt}}{dC_L} \frac{S_t l_t}{S_w c} \eta_t + \frac{dC_{T_1}}{dC_L} \frac{d_1}{c} \sin(\theta_1) + \frac{dC_{T_2}}{dC_L} \frac{d_1}{c} \sin(\theta_2)$$